The Astrophysical Journal, 909:40 (21pp), 2021 March 1 https://doi.org/10.3847/1538-4357/abd6e5
© 2021. The American Astronomical Society. All rights reserved.

Tracing the Formation History of Giant Planets in Protoplanetary Disks with Carbon, Oxygen, Nitrogen, and Sulfur

D. Turrini[1], E. Schisano[1], S. Fonte[1], S. Molinari[1], R. Politi[1], D. Fedele[2,3], O. Panić[4], M. Kama[5,6], Q. Changeat[5], and G. Tinetti[5]

[1] INAF—Istituto di Astrofisica e Planetologia Spaziali (INAF-IAPS), Via del Fosso del Cavaliere n. 100, I-00133, Rome, Italy; diego.turrini@inaf.it
[2] INAF, Osservatorio Astrofisico di Torino, Via Osservatorio 20, I-10025, Pino Torinese, Italy
[3] INAF—Osservatorio Astrofisico di Arcetri, Largo E. Fermi 5, I-50127 Firenze, Italy
[4] School of Physics and Astronomy, E.C. Stoner Building, University of Leeds, Leeds LS2 9JT, UK
[5] Department of Physics and Astronomy, University College London, London, WC1E 6BT, UK
[6] Tartu Observatory, University of Tartu, Observatooriumi 1, 61602 Tõravere, Estonia
Received 2020 July 10; revised 2020 December 22; accepted 2020 December 24; published 2021 March 3

Abstract

The composition of giant planets is imprinted by their migration history and the compositional structure of their hosting disks. Studies in recent literature have investigated how the abundances of C and O can constrain the formation pathways of giant planets forming within few tens of au from a star. New ALMA observations, however, suggest planet-forming regions possibly extending to hundreds of au. We explore the implications of these wider formation environments through *n*-body simulations of growing and migrating giant planets embedded in planetesimal disks, coupled with a compositional model of the protoplanetary disk where volatiles are inherited from the molecular cloud and refractories are calibrated against extrasolar and Solar System data. We find that the C/O ratio provides limited insight on the formation pathways of giant planets that undergo large-scale migration. This limitation can be overcome, however, thanks to nitrogen and sulfur. Jointly using the C/N, N/O, and C/O ratios breaks any degeneracy in the formation and migration tracks of giant planets. The use of elemental ratios normalized to the respective stellar ratios supplies additional information on the nature of giant planets, thanks to the relative volatility of O, C, and N in disks. When the planetary metallicity is dominated by the accretion of solids $C/N^* > C/O^* > N/O^*$ (* denoting this normalized scale), otherwise $N/O^* > C/O^* > C/N^*$. The S/N ratio provides an additional independent probe into the metallicity of giant planets and their accretion of solids.

Unified Astronomy Thesaurus concepts: Planet formation (1241); Protoplanetary disks (1300); Metallicity (1031); Chemical abundances (224); Abundance ratios (11); Extrasolar gaseous giant planets (509)

1. Introduction

The formation of giant planets is one of the defining milestones in the life of planetary systems, and plays a fundamental role in shaping their architecture and habitability (e.g., Morbidelli & Raymond 2016, and references therein). Understanding the formation pathways of giant planets, however, is proving quite a challenging task, particularly in terms of answering the following questions: where do they form, and how and when do they acquire their final orbits?

The orbital architectures of the known exoplanetary systems, with their large population of giant planets at a fraction of au from the star, provide a strong argument that migration processes play a crucial role in the formation pathways of these planets. A prime mechanism for their migration is generally identified in the interaction and exchange of angular momentum with the protoplanetary disk (e.g., Nelson 2018, and references therein), which also allows the migrating planet to encounter and capture more significant quantities of solid material than it would otherwise (e.g., Turrini et al. 2015; Shibata & Ikoma 2019; Shibata et al. 2020, and references therein).

Population studies of the metallicities of giant planets, both around other stars (Thorngren et al. 2016; Wakeford et al. 2017) and in our Solar System (e.g., Atreya et al. 2018, and references therein), have revealed widespread super-stellar enrichments in high-*Z* elements in their H/He-dominated gaseous envelopes, consistent with the coupling between early disk-driven migration and enhanced accretion of solid material. The highest estimated metallicities, in particular, can currently be explained only by invoking extensive disk-driven migration from the outer regions of protoplanetary disks, coupled with equally extensive accretion of planetesimals (Shibata et al. 2020).

This scenario appears to be supported by the possible large extension of the planet-forming region in protoplanetary disks suggested by recent observations with ALMA (e.g., ALMA Partnership et al. 2015; Isella et al. 2016; Fedele et al. 2017, 2018; Andrews et al. 2018 and references therein; Long et al. 2018). These observations revealed the widespread presence of morphological features ascribed to the presence of giant planets from several tens to a few hundreds of au from their central stars. However, those very observations also revealed that giant planets could remain at such distances from their stars for several millions of years, raising the question of whether disk-driven migration is a common occurrence or not.

Furthermore, the architecture of a large fraction of exoplanetary systems shows signatures of a chaotic dynamical evolution (Limbach & Turner 2015; Laskar & Petit 2017; Zinzi & Turrini 2017; Turrini et al. 2020), suggesting that not all giant planets have their dynamical histories shaped by early disk-driven migration, but they can reach their final orbits at a later time as a result of planet–planet scattering events, chaotic dynamics, or a combination of early and late migration. Due to these uncertainties, metallicity alone is not enough to fully disclose a giant planet's formation history, aside from the most extreme cases.

The information provided by the atmospheres of giant planets on their interior composition allows for breaking this degeneracy; for recent discussions, see, e.g., Madhusudhan et al. (2016), Tinetti et al. (2018), Turrini et al. (2018), Madhusudhan (2019), and references therein. In the coming years, the task of characterizing in detail the atmospheric composition of exoplanets will be first undertaken by the James Webb Space Telescope (JWST; Cowan et al. 2015). Soon after, the space mission Ariel of the European Space Agency will address this task in a systematic way for a sample of several hundreds of exoplanets (Tinetti et al. 2018).

Since the early work of Öberg et al. (2011), several studies have been devoted to understanding the link between the abundances of the two most abundant high-Z elements, carbon (C) and oxygen (O), and the planetary formation process; for more recent discussions, see, e.g., Madhusudhan et al. (2016), Mordasini et al. (2016), Booth & Ilee (2019), Cridland et al. (2019), and references therein. Recently, a few studies have taken a first look at nitrogen (N), as well (Bosman et al. 2019; Öberg & Wordsworth 2019). However, the implications of formation regions extending as far from the star as ALMA reveals, as well as those of accreting large amounts of high-Z material across many of the compositional regions inside disks, remain poorly understood.

The goal of this study is, therefore, twofold. On the one hand, we want to investigate the information provided by the C/O ratio when the migration tracks of giant planets extend over tens or hundreds of au and cross many of the diverse compositional regions in protoplanetary disks. On the other hand, we want to expand our suite of compositional tracers to nitrogen (N) and sulfur (S) to improve our understanding of the link between planetary composition and formation process.

The rest of this work is organized as follows. In Section 2, we detail the dynamical and compositional models at the basis of our study. In Section 3, we present the outcomes of the investigated scenarios in terms of planetary metallicity and abundance ratios of the four elements under study. In Section 4, we discuss the additional information that is provided by the combined use of planetary and stellar elemental ratios, as well as the implications of the uncertainty on the volatility of N in protoplanetary disks. Finally, in Section 5, we draw the conclusions of our work and summarize the applications of our results.

2. Numerical and Compositional Model

Our work is based on two complementary modeling efforts. The first one is a set of detailed n-body simulations, each tracking the dynamical evolution of planetesimals in response to the growth and migration of a forming giant planet, sampling different formation regions in the protoplanetary disk. The second is a compositional model for the solids and the gas in the protoplanetary disk, accounting for the information provided by both solar and extrasolar materials. The n-body simulations were performed with the Mercury-ARχES software (Turrini et al. 2019), briefly described in Section 2.1. Details on the treatment of the physical processes included in the n-body simulations are provided in Sections 2.2, 2.3, and 2.4. The compositional model used to analyze the outcomes of the n-body simulations is described in Section 2.5.

2.1. The n-body Code Mercury-ARχES

To simulate the formation and migration of the giant planet and its interactions with the planetesimal disk, we used Mercury-ARχES (Turrini et al. 2019), a high-performance implementation of the hybrid symplectic algorithm of the Mercury 6 software from Chambers (1999). Symplectic algorithms (Kinoshita et al. 1991; Wisdom & Holman 1991) are a family of leapfrog integration schemes that are well-suited to simulating the evolution of planetary systems over long timescales, as they show no long-term accumulation of the energy error while being about an order of magnitude faster than conventional n-body algorithms.

The energy conservation property of symplectic algorithms is guaranteed as long as the hierarchical structure of the dynamical system is not violated: for planetary systems, this means that the dynamical evolution of the bodies should be dominated by the gravitational field of the central star. This condition is violated during close encounters between planetary bodies, in principle making symplectic algorithms unsuitable for studies of planetary formation.

Hybrid symplectic algorithms allow this problem to be circumvented by switching to high-precision non-symplectic integration schemes for the duration of the close encounter while reproducing the dynamical evolution of the involved bodies (Chambers 1999). To guarantee high numerical stability and accuracy, Mercury's hybrid symplectic algorithm uses the Bulirsh–Stoer integration scheme to compute the Keplerian motion of the bodies undergoing close encounters (Chambers 1999). Mercury-ARχES implements a high-performance version of the hybrid symplectic scheme of Mercury, parallelized and vectorized with OpenMP to take advantage of the SIMD (single instruction, multiple data) capabilities of modern multicore architectures.

Mercury-ARχES further expands the hybrid symplectic algorithm of Mercury with the inclusion of the following effects on the dynamical evolution of the simulated system (see the relevant sections for details on their implementation):

1. The mass growth and planetary radius evolution of forming giant planets (Section 2.2)
2. Orbital migration during the different phases of the formation of giant planets (Section 2.2)
3. The exciting effect of the self-gravity of an axisymmetric protoplanetary disk on the motion of planetary bodies (Section 2.3)
4. The damping effects of aerodynamic drag on the motion of the planetesimals due to the disk gas (Section 2.3)

For improved numerical stability and accuracy, the symplectic algorithm of Mercury-ARχES takes advantage of the WHFast library (Rein & Tamayo 2015) to compute the Keplerian drift of the planetary bodies in place of Mercury's original subroutines.

2.2. Growth and Migration of the Giant Planets

The growth of the giant planet in each n-body simulation follows the growth tracks from Lissauer et al. (2009), Bitsch et al. (2015), and D'Angelo et al. (2021) using the parametric approach from Turrini et al. (2011, 2019). For consistency with these works, we adopted a common formation time of 3 Myr for all giant planets in our simulations. The orbits of the giant planets lie on the midplane of the protoplanetary disk (i.e., they

have inclination $i = 0°$) and have initial eccentricities of the order of 10^{-3} to account for the damping effects of the tidal gas drag on the growing planetary cores (Cresswell & Nelson 2008).

During the first $\tau_c = 2$ Myr, the giant planet accretes its core and extended atmosphere (Lissauer et al. 2009; D'Angelo et al. 2021), its overall mass (M_P) growing from an initial value of $M_0 = 0.1\,M_\oplus$ (a Mars-size planetary embryo) to the critical value $M_c = 30\,M_\oplus$ (equally shared between core and atmosphere) as:

$$M_P = M_0 + \left(\frac{e}{e-1}\right)(M_c - M_0)(1 - e^{-t/\tau_c}). \quad (1)$$

After the critical mass value M_c is reached, the giant planet enters its runaway gas accretion phase and its mass evolves over the following 1 Myr as:

$$M_P = M_c + (M_F - M_c)(1 - e^{-(t-\tau_c)/\tau_g}), \quad (2)$$

where M_F is the final planetary mass, for which we adopted a common value of $M_F = 1$ Jovian mass ($M_J = 317.8\ M_\oplus$). The e-folding time $\tau_g = 10^5$ yr was chosen based on the hydrodynamical simulations of Lissauer et al. (2009), Coradini et al. (2010), D'Angelo et al. (2010), D'Angelo et al. (2021), and references therein.

The physical radius of the growing giant planet (R_P) evolves alongside the planetary mass following the approach described by Fortier et al. (2013), which is based in turn on the hydrodynamic simulations of Lissauer et al. (2009). During the initial phase, described by Equation (1), when the planetary core is growing its extended atmosphere, the physical radius evolves as:

$$R_P = \frac{GM_P}{c_s^2/k_1 + (GM_P)/(k_2 R_H)}, \quad (3)$$

where G is the gravitational constant, M_P is the instantaneous mass of the giant planet, c_s is the sound speed in the protoplanetary disk at the orbital distance of the planet, R_H is the planetary Hill's radius, $k_1 = 1$, and $k_2 = 1/4$ (Lissauer et al. 2009).

Once the giant planet enters its runaway gas accretion phase described by Equation (2) (i.e., for $t > \tau_c$), the gravitational infall of the gas causes the planetary radius to shrink and evolve as:

$$R_P = R_c - \Delta R(1 - \exp^{-(t-\tau_c)/\tau_g}), \quad (4)$$

where R_c is the planetary radius at $\tau_c = 2$ Myr, i.e., the end of the extended atmosphere phase described by Equation (3), and $\Delta R = R_c - R_I$ is the decrease of the planetary radius during the gravitational collapse of the gas. We adopted a final value of the planetary radius $R_I = 1.6\,R_J = 1.15 \times 10^5$ km (Lissauer et al. 2009; Podolak et al. 2020) to account for the inflation of the young giant planet.

The migration of the growing giant planet due to its interactions with the surrounding protoplanetary disk is modeled through a semi-analytical approach that reproduces the realistic nonisothermal migration tracks from the population synthesis models by Mordasini et al. (2015). These models directly account for the interactions between a growing protoplanet and its evolving host circumstellar disk that are not included in our n-body simulations or our parameterization of the disk environment.

As discussed in Mordasini et al. (2015) and references therein, the seeds of growing protoplanets will quickly migrate (either inward or outward, depending on their position in the disk) toward the nearest convergence point, a region of zero net torque due to disk–planet interactions. Once the convergence point is reached, the protoplanet will slowly migrate inward due to Type I migration following the inward drift of the convergence point caused by the evolution of the disk (Mordasini et al. 2015).

The growth of the protoplanet will eventually cause it to exit the convergence point and enter a faster regime of Type I migration. Once the protoplanet becomes massive enough to open a gap in the disk, it will transition into the slower Type II migration regime. The migration tracks of Mordasini et al. (2015) show how, after the protoplanet reaches the convergence point, this sequence of different phases takes the form of an initial linear migration regime, associated with the slow migration with the convergence point, followed by a power-law migration regime, encompassing the fast Type I migration and the transition to Type II migration.

These linear and power-law regimes are reproduced in the n-body simulations using a piecewise approach based on the analytical treatments of Hahn & Malhotra (2005) and Walsh et al. (2011). This approach allows for a computationally efficient parameterization of the dynamical behavior of the growing giant planet and simplifies the exploration of the combined effects of planetary growth and migration. Future studies will address the implications of physically self-consistent treatments of the coupling between disk evolution, planetary growth, and migration for the planetesimal accretion history.

During the growth of the planetary core to the critical value (M_C in Equation (1)), the giant planet undergoes initial slow Type I migration governed by the following drift rate Δv_1 (Hahn & Malhotra 2005; Walsh et al. 2011):

$$\Delta v_1 = \frac{1}{2}\frac{\Delta a_1}{a_p}\frac{\Delta t}{\tau_c} v_P, \quad (5)$$

where Δa_1 is the radial displacement of the giant planet during its core growth, v_p and a_p are its current orbital velocity and semimajor axis, respectively, $\tau_c = 2$ Myr is the characteristic time governing the mass growth of the core used in Equation (1), and Δt is the time step used in the n-body simulations.

Once the core reaches its critical mass and the phase of runaway gas accretion begins, the giant planet first enters the faster Type I migration to later transition to the slower Type II migration. During this phase, its orbital evolution is governed by the following drift rate Δv_2 (Hahn & Malhotra 2005):

$$\Delta v_2 = \frac{1}{2}\frac{\Delta a_2}{a_p}\frac{\Delta t}{\tau_g}\exp^{-(t-\tau_c)/\tau_g} v_P, \quad (6)$$

where Δa_2 is the radial displacement of the giant planet during its runaway gas accretion, $\tau_g = 10^5$ yr is the characteristic time governing the gas accretion used in Equation (2), and all other parameters are the same as those in Equation (5).

It is worth noting that the dynamical behavior described by Equation (6) is analogous to that adopted by Shibata et al. (2020) in their simulations; however, they did not model the initial growth of the core and the associated migration described by Equation (5). In addition, the characteristic

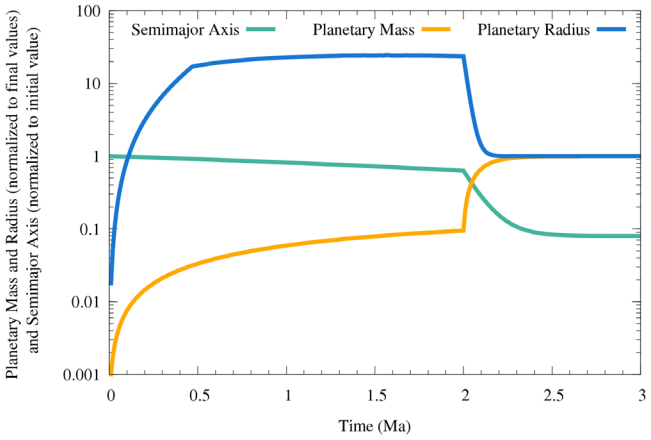

Figure 1. Normalized growth and migration tracks from the scenario where the giant planet starts forming at 5 au. Growth tracks of both mass and radius are normalized to the final mass (1 M_J) and radius (1.6 R_J) of the giant planet. The migration track is instead normalized to the initial semimajor axis (5 au) of the giant planet.

timescale τ_g adopted in this work is the same as the one in their reference case, allowing for an easier comparison with their results in terms of planetesimal accretion.

As the characteristic migration timescales in Equations (5) and (6) are fixed, the main free parameters characterizing the migration tracks are the displacements Δa_1 and Δa_2. We considered a total of six migration scenarios, with the core of the giant planet starting its growth at 5, 12, 19, 50, 100, and 130 au, respectively. In all simulations, the giant planet ends its migration at 0.4 au. As we detail in Section 2.4, this final position of the giant planet is chosen for reasons of computational efficiency. Still, the giant planet could actually end its migration anywhere within 0.4 au without its planetesimal accretion history being affected.

To cross-calibrate the migration tracks from Mordasini et al. (2015) resulting from Equations (5) and (6) with the joint growth and migration tracks of Bitsch et al. (2015), we defined the values of Δa_1 and Δa_2 such that they account for 40% and 60%, respectively, of the total radial displacement the giant planet experiences during its formation in each simulation. In all scenarios, the initial position of the giant planet is implicitly assumed to coincide with that of a convergence point in the disk. An example of the growth and migration tracks of the giant planet resulting from Equations (1)–(6) is shown in Figure 1.

To verify that the adopted migration tracks are not associated with unrealistic migration rates, we compared them with the constraints on Jupiter's migration rates needed to reproduce the observed asymmetry among its Trojan populations (Pirani et al. 2019). As discussed by Pirani et al. (2019), Jupiter's migration rate at the onset of the rapid gas accretion, when its mass was about 30 $M_\oplus$, should have been comprised between about 30 and 300 au Myr^{-1} for the planet to capture Trojan populations consistent with current estimates.

The migration rates experienced by the giant planet during the first e-folding time of the power-law migration regime of Equation (6) range between 20 and 500 au Myr^{-1}. As a result, the scenarios where the giant planet starts between 12 and 50 au are consistent with the constraints on Jupiter's migration rate reported by Pirani et al. (2019). The scenario where the giant planet starts at 5 au is about 1/3 slower than the lower bound of the interval of values from Pirani et al. (2019), while the scenarios where the giant planet starts at 100 and 130 au are about 1/3 and 2/3 faster, respectively, than the upper bound on Jupiter's migration rate.

As a further validation, we compared the migration rate of the giant planet over the following four e-folding times (i.e., between 2.1 and 2.5 Myr), assumed as an upper limit to the Type II migration rate, with the nominal Type II migration rate associated with our parameterization of the protoplanetary disk (see Section 2.3). The Type II migration rate in our scenarios thus ranges between 3 and 70 au Myr^{-1}. Following Armitage (2009) and adopting the same value of $\alpha = 0.0053$ as Bitsch et al. (2015) the nominal Type II migration rate would be about 60 au Myr^{-1}, with the value oscillating between 1 au Myr^{-1} and 100 au Myr^{-1} for α comprised between 10^{-4} and 10^{-2}, respectively.

2.3. Protoplanetary Disks and Dynamical Effects of Gas

To explore the implications of wide planet-forming regions on the final compositional features of giant planets, we modeled our template disk over one of the largest and best-characterized protoplanetary disks to date, the one surrounding the 1.9 $M_\odot$ star HD 163296 (Isella et al. 2016; Turrini et al. 2019). As the focus of our compositional modeling is on solar analog stars (see Section 2.5), we scaled down HD 163296's observed gas surface density profile (Isella et al. 2016) by a factor of 1.6 to obtain a total mass of the disk equal to the mass of a Minimum Mass Solar Nebula (MMSN; Hayashi 1981) with similar extension.

As a result, the central star in all our simulations has a mass of 1 $M_\odot$ and is surrounded by a protoplanetary disk with mass $M_\mathrm{D} = 0.053\ M_\odot$ whose gas surface density profile on the midplane is:

$$\Sigma_{\mathrm{gas}}(r) = \Sigma_0 \left(\frac{r}{165\ \mathrm{au}}\right)^{-0.8} \exp\left[-\left(\frac{r}{165\ \mathrm{au}}\right)^{1.2}\right], \quad (7)$$

where $\Sigma_0 = 3.3835\ \mathrm{g\ cm}^{-3}$. This gas surface density profile results in a disk rapidly truncating at about 500 au. We adopted a value of 0.1 au as the disk inner edge in our simulations.

The temperature radial profile in the midplane of our template disk is characterized by the same radial dependency as the disk midplane temperature estimated for HD 163296 (Isella et al. 2016). We calibrated the temperature T_0 at 1 au on the one estimated for the MMSN (Hayashi 1981):

$$T(r) = T_0 \left(\frac{R}{1\ \mathrm{au}}\right)^{-1/2} K, \quad (8)$$

where $T_0 = 280$ K. This results in a warm protoplanetary disk where the different snow lines are distributed between ~3 and ~100 au (see Section 2.5 for details).

The density and temperature profiles of the disk from Equations (7) and (8) allow us to compute the damping effects of the gas on the dynamical evolution of the planetesimals using the treatment from Brasser et al. (2007) and references therein. The drag acceleration F_D is expressed by:

$$F_D = \frac{3}{8} \frac{C_D}{r_p} \frac{\rho_g}{\rho_p} v_r^2, \quad (9)$$

where C_D is the gas drag coefficient, ρ_g is the local density of the gas, ρ_p and r_p are the density and radius of the

planetesimals, respectively, and v_r is the relative velocity between gas and planetesimals.

The gas drag coefficient C_D of each planetesimal is computed following the treatment described by Nagasawa et al. (2019) as a function of the Reynolds (Re) and Mach (Ma) numbers, coupling the individual drag coefficients to the specific orbit of the planetesimal and to the local disk environment:

$$C_D = \left[\left(\frac{24}{Re} + \frac{40}{10 + Re}\right)^{-1} + 0.23Ma\right]^{-2} + \frac{2 \cdot (0.8k + Ma)}{1.6 + Ma}, \quad (10)$$

where k is a factor with a value of 0.4 for $Re < 10^5$ and 0.2 for $Re > 10^5$ (Nagasawa et al. 2019).

To account for the formation of a gap in the protoplanetary disk around the growing giant planet after the onset of its runaway gas accretion phase (i.e., for $t > \tau_c$), we adopted the same approach as Marzari (2018) and assumed the giant planet to be surrounded by a gap with width:

$$W_{\rm gap} = C \cdot R_H, \quad (11)$$

where the numerical proportionality factor $C = 8$ is from Isella et al. (2016). The gas density $\Sigma_{\rm gap}(r)$ inside the gap is assumed to evolve over time with respect to the local unperturbed gas density $\Sigma(r)$ as:

$$\Sigma_{\rm gap}(r) = \Sigma(r) \cdot \exp\left[-(t - \tau_c)/\tau_g\right], \quad (12)$$

where τ_c and τ_g are the same as in Equations (1) and (2).

The disk density profile from Equation (7) also allows us to compute the dynamical excitation of the planetesimals due to the effects of the disk self-gravity through the analytical treatment for thin disks from Ward (1981). Fontana & Marzari (2016) showed that the perturbations due to the disk self-gravity computed with this analytical treatment are in good agreement with the perturbations computed using hydrodynamic simulations for axisymmetric disks. The effects on the self-gravity potential of nonaxisymmetric density structures in the disk (see, e.g., Gratton et al. 2019, and references therein) are not included into this treatment and would require dedicated hydrodynamic simulations that are beyond the scope of this work.

Here, we follow the approach of Nagasawa et al. (2019) and focus only on the leading term of the force due to self-gravity ($F_{\rm SG}$):

$$F_{\rm SG} = 2\pi G\Sigma(r) \sum_{n=0}^{\infty} A_n \frac{(1 - k)(4n + 1)}{(2n + 2 - k)(2n - 1 + k)}, \quad (13)$$

where $k = 0.8$ is the exponent of the power law part of Equation (7) and $A_n = [(2n)!/2^{2n}(n!)^2]^2$ (Ward 1981; Marzari 2018).

For this value of k, the sum on the right-hand side of Equation (13) converges to the value -0.754126, which means that the equation can be rewritten in more compact form as:

$$F_{\rm SG} = Z\pi G\Sigma(r), \quad (14)$$

where $Z = -1.508252$. It has been shown by Fontana & Marzari (2016) that, while the focus of Nagasawa et al. (2019) on the leading perturbation term is computationally efficient, it produces accurate results only when the planetary bodies are distant from both the inner and the outer edges of the disk. For those bodies not satisfying these conditions, additional terms need to be considered in Equation (13) (Ward 1981; Fontana & Marzari 2016; Marzari 2018).

While in our simulations the planetesimals are always well inside the outer edge of the disk (at ≈500 au), the same does not apply to the inner edge of the disk (at 0.1 au) at the end of the orbital migration of the giant planets. However, in the inner regions of the disk, the dynamical evolution of the planetesimals is dominated by gas drag, which quickly and efficiently cancels out any excitation effect due to the disk self-gravity. Numerical experiments have shown no appreciable difference in the dynamical evolution of the planetesimals when the additional terms required to account for the effects of the inner disk edge are included. As a result, we maintained the same approach as Nagasawa et al. (2019) for reasons of computational efficiency.

2.4. Planetesimal Disk and Time Step of the Simulations

We simulated the planetesimal disk as a swarm of dynamical tracers, each possessing an inertial mass but no gravitational mass. The lack of gravitational mass means that each tracer is affected by the gravitational potential of the star, the growing giant planet, and the disk, but the tracers do not affect those objects or each other. At the same time, each tracer possesses an inertial mass that determines the way it is affected by gas drag.

To compute the inertial mass of the dynamical tracers, we adopted a fixed radius of $r_p = 50$ km, i.e., the characteristic size of planetesimals formed by pebble accretion (e.g., Klahr & Schreiber 2016). We adopted density values of $\rho_{\rm rock} = 2.4\ {\rm g\ cm^{-3}}$ for the rock-dominated planetesimals inside the water snow line and $\rho_{\rm ice} = 1\ {\rm g\ cm^{-3}}$ for the ice-rich planetesimals beyond it (see Section 2.5 for details on the planetesimal composition).

The value of $\rho_{\rm rock}$ has been chosen as a compromise between the measured densities of volatile-poor and volatile-rich asteroids (e.g., Britt et al. 2002; Carry 2012, and references therein). The value of $\rho_{\rm ice}$ has been chosen instead as a compromise between the measured densities of comets (0.4–0.6 g cm^{-3}; see, e.g., Brasser et al. (2007) and references therein, as well as Jorda et al. (2016)) and that of the larger (≈200 km in diameter), ice-rich, captured trans-Neptunian object Phoebe (1.63 g cm^{-3}; see Porco et al. (2005)).

The dynamical tracers representing the planetesimals are distributed randomly in semimajor axis, adopting a uniform probability distribution between 1 and 150 au (see below for a discussion of these boundaries) with a spatial density of 2000 tracers/au. The initial orbital eccentricities and inclinations (in radians) of the planetesimals are distributed randomly between 0 and 10^{-2} (Weidenschilling 2008).

As we do not model the growth of the core of the giant planet from the surrounding material directly, when generating the initial conditions of the planetesimal disk, planetesimals are prevented from populating a radial region equivalent to the feeding zone of the giant planet, to account for the local depletion of material and avoid overestimating the planetesimal accretion by the envelope.

This feeding zone is centered on the initial orbital position of the giant planet, and its width is defined through the

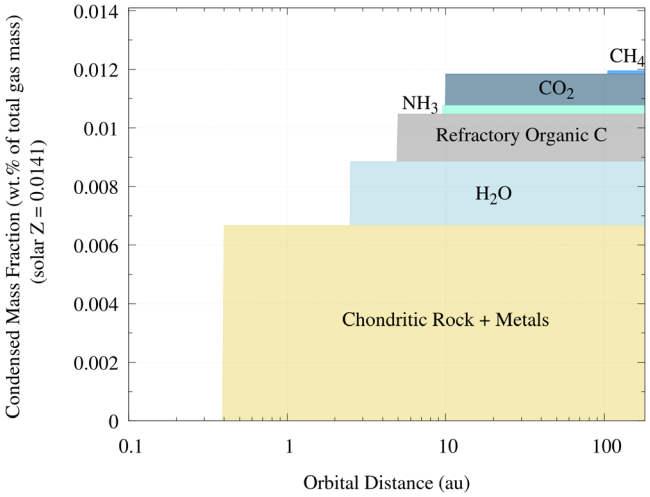

Figure 2. Mass fraction of solid material as a function of the distance from the star in our template protoplanetary disk. Mass fraction is expressed with respect to the total mass of gas, assuming a solar composition for the latter. The mass fraction of condensed material is always lower than the protostellar Z, as some elements (Ne) and molecules (CO and N_2) never condense in our disk (see main text and Table 3 for further details).

relationship

$$W_{\rm iso} = b \cdot R_{H-{\rm iso}}, \tag{15}$$

where $R_{H-{\rm iso}}$ is the Hill's radius of a planetary core with an isolation mass of $M_{\rm iso} = 15\ M_{\oplus}$ (the critical mass used in Section 2.2 without the contribution of the gaseous envelope) and $b = 4$ (see Kokubo & Ida 2000; D'Angelo et al. 2010, and references therein).

The upper boundary of the planetesimal disk at 150 au accounts for the inward drift of dust and pebbles across the formation of planetesimals due to their dynamical coupling with the gas. The inward drift of dust and pebbles results in a higher concentration of condensed materials in the inner regions of protoplanetary disks at the expense of their outer regions, which gradually deplete.

The observations of multiple circumstellar disks confirms the efficiency of this process, revealing that the gas can extend between ≈2 to more than 4 times farther out than the dust (e.g., Isella et al. 2016; Ansdell et al. 2018; Facchini et al. 2019). In particular, the protoplanetary disk surrounding HD 163296, which our template disk is based on, is characterized by gas extending to about 500 au, while dust is detected only up to 250 au (Isella et al. 2016).

To account for the increased concentration of solid material in the inner disk and depletion in the outer disk, we follow the approach of Mordasini et al. (2009) and adopt a solids concentration factor ξ. The solids concentration factor ξ is defined as:

$$\xi = \begin{cases} 2 & x \leqslant 150\ {\rm au} \\ 0 & x > 150\ {\rm au} \end{cases}. \tag{16}$$

This is a conservative choice in terms of the observed range of values (Isella et al. 2016; Ansdell et al. 2018; Facchini et al. 2019) that mimics the HD 163296's radial behavior of gas and dust.

The solids concentration factor ξ is used in conjunction with the mass fraction of condensed material Z_i (shown in Figure 2 and described in Section 2.5 and Table 3) to compute the radial distribution of solids

$$\Sigma_{\rm solids}(r) = \Sigma_{\rm gas}(r)\xi(r)Z_i(r), \tag{17}$$

where the product of ξ and Z_i represents the local solids-to-gas ratio. Integrating Equation (17) over a given annular region of the disk allows the local mass of the planetesimal disk to be computed.

While our template protoplanetary disk extends down to 0.1 au (see Section 2.3), the initial inner boundary of the planetesimal disk is set to 1 au in the n-body simulations for reasons of computational efficiency. This allows us to adopt a time step $dt = 15$ days (i.e., 1/24 of the orbital period of the innermost dynamical tracer) in Mercury-Arχes symplectic algorithm and limit the computational load of the simulations. The inclusion of planetesimals between 0.1 and 1 au would require the use of smaller time steps, proportionally increasing the computational load. However, numerical experiments performed with planetesimal disks extending down to 0.4 au showed that tracers inside 1 au do not contribute to the accretion history of the giant planet in the growth and migration tracks we considered.

Because planetary migration always stops at 0.4 au in our simulations (see Section 2.2), near the end of its formation track, the giant planet enters the orbital region where the time step of $dt = 15$ days does not allow for accurate reproduction of its dynamical evolution. To address this issue, we follow an approach similar to that of Jurić & Tremaine (2008). When the giant planet approaches 1 au, we decrease the time step to $dt = 2.4$ days (1/25 of the orbital period at an orbital distance of 0.3 au) in order to accurately resolve its orbital evolution down to its final semimajor axis.

While the high numerical stability of the WHFAST Kepler solver (Rein & Tamayo 2015) allows for this transition to occur seamlessly, for increased accuracy, MERCURY-ARχES also implements a hybrid approach during the time step when the transition in dt occurs. As a result, the Keplerian orbital motions of all bodies within 1 au are computed using the Bulirsch–Stoer integrator of MERCURY (Chambers 1999) during this time step.

In each simulation, we recorded the flux of impacts between the dynamical tracers representing the planetesimals and the giant planet, whose collisional cross section matches the geometrical one associated with the physical radius computed as described in Section 2.2. In principle, this treatment of the collisional cross section might result in overestimating the flux of planetesimals impacting the giant planet. Due to their relatively large radius assumed in this work, in fact, planetesimals encountering the giant planet with high impact parameters may cross only its less dense atmospheric region and escape capture, resulting in a smaller effective collisional cross section of the giant planet (e.g., Fortier et al. 2013, and references therein).

It should be noted, however, that the adopted treatment neglects effects linked to the presence and temperature of gas in a circumplanetary disk (e.g., Coradini et al. 2010, and references therein) and in the Hill's sphere of the giant planet (Szulágyi et al. 2016) that could increase the efficiency of the capture process. This could be achieved by enhancing the efficiency of planetesimal ablation and break-up due to the ram pressure of the gas (see also Mordasini et al. 2015; Vazan et al. 2015; Podolak et al. 2020), by allowing for planetesimal capture in decaying circumplanetary orbits (as implicitly done

in the model of Shibata et al. (2020)), or via the combined action of these effects over multiple planetary encounters (Podolak et al. 2020).

In particular, recent results from Podolak et al. (2020) show that the planetesimal capture efficiency of growing giant planets quickly becomes independent of the planetesimal size as soon the mass of the gaseous envelope reaches a few Earth masses (see below for further discussion). As a result, large planetesimals with diameters of 100 km, like those considered in our simulations, will be accreted with the same efficiency as small planetesimals with diameters of 1 km, for which previous studies revealed that the effective collisional radius of the giant planet closely matches its physical radius (D'Angelo et al. 2014; Mordasini et al. 2015; Vazan et al. 2015).

We tested how planetesimal accretion scales with the collisional radius of the giant planet by simulating a scenario where the giant planet starts at 130 au while considering a collisional radius equal to 75% of the values obtained by Equations (3) and (4). The results we obtained show that the planetesimal capture efficiency is about 80% compared with the one obtained in the nominal simulation. This suggests that the roles of multiple planetary encounters and of the gravitational focusing by the growing planet partly compensate for the reduced collisional cross section and that the planetesimal accretion efficiency should scale almost linearly with the planetary radius.

Finally, recent hydrodynamic simulations (D'Angelo et al. 2021) report planetary radii about ∼25% larger for the growing giant planet, both during the extended envelope phase (see Equation (3)) and across the gravitational infall (see Equation (4)), than those resulting from the hydrodynamic simulations of Lissauer et al. (2009) considered in this work. As a result, the adopted treatment of the collisional cross section of the giant planet should represent a reasonable and conservative approximation for the scope of this work. We refer the readers to Section 4 for further discussion of this issue.

Following the approach described in Turrini et al. (2011, 2012), Turrini (2014), and Turrini & Svetsov (2014), from the knowledge of their respective formation regions, we can associate each dynamical tracer impacting on the giant planet with a mass flux of planetesimals. Specifically, integrating the solids surface density profile from Equation (17) over a given orbital annular region of the disk allows for the computation of the total mass of solids, and hence planetesimals, it contains.

From the physical radius and density of the planetesimals represented by each dynamical tracer, we can compute their masses. Dividing the total mass of solids in a given orbital annular region of the disk by the individual mass of its planetesimals allows for the total number of planetesimals populating it to be computed. Dividing the population of planetesimals in that annular region by the number of dynamical tracers it contains, we can associate each dynamical tracer with the swarm of planetesimals it represents. From the recorded fluxes of impacting tracers, it is then straightforward to compute the mass flux of planetesimals on the giant planet.

Recent studies (D'Angelo et al. 2014; Mordasini et al. 2015; Vazan et al. 2015; Podolak et al. 2020) indicate that, as the gaseous envelope of the giant planet becomes more massive than a few Earth masses, accreted planetesimals efficiently dilute into it, independent of planetesimal size and composition, due to the combined effects of break-up and ablation. Because of the gap we enforce around the giant planet in the initial planetesimal distribution (see Equation (15)), this condition is always satisfied in our simulations before the onset of planetesimal accretion. As a result, all high-Z material accreted by the giant planet is assumed to remain mixed in the gaseous envelope (see also Podolak et al. 2020).

It should be noted, however, that the partitioning and distribution of high-Z material in the interiors and atmospheres of giant planets, both at the end of the formation process and after a few Gyrs of interior evolution, is still a matter of debate. This uncertainty holds true even in the well-studied cases of Jupiter and Saturn in our own Solar System, notwithstanding detailed *in situ* measurements provided by the Galileo, Cassini, and Juno missions; see Atreya et al. (2018), Helled (2018), Stevenson (2020), and references therein for recent in-depth discussions.

The combination of the data provided by the Galileo and Juno missions for Jupiter suggest the diffuse presence of high-Z elements both in the gaseous envelope and the atmosphere of the giant planet, although little to no information is available on their possible compositional homogeneity or radial gradients (see Stevenson 2020, and references therein). In this work, the high-Z material accreted through planetesimals is assumed to be uniformly distributed into the envelope, and we leave a more detailed exploration of this issue to future work. We refer the readers to Section 4 for a discussion of the implications of a nonuniform distribution of the high-Z material.

2.5. Compositional Model of the Disk and the Planetesimals

As introduced in Section 2.3, we focus our study on host stars that are solar analogs both in terms of mass (1 $M_{\odot}$) and composition. The protostellar elemental abundances of both star and disk are computed from the photospheric abundances from Asplund et al. (2009) integrated with the updated values from Scott et al. (2015a, 2015b) and corrected for the sinking of He and the high-Z elements as described in Asplund et al. (2009). The values $X = 0.7148$, $Y = 0.2711$, and $Z = 0.0141$ characterize the resulting composition of both star and disk in terms of mass fractions of H, He and heavy elements, respectively.

Our compositional model focuses on four tracing elements: carbon (C), oxygen (O), nitrogen (N), and sulfur (S). To characterize their distribution across the different phases (gas, rock, organics, ice) in the protoplanetary disk, we follow an approach conceptually similar to those of previous works (e.g., Johnson et al. 2012; Thiabaud et al. 2014; Marboeuf et al. 2014a, 2014b; Mordasini et al. 2016; Cridland et al. 2019) and combine the information provided by meteoritic abundances (Lodders 2010; Palme et al. 2014), extrasolar planetary material (Doyle et al. 2019; Kama et al. 2019), the interstellar medium (Palme et al. 2014; Bergin et al. 2015; Mordasini et al. 2016), and astrochemical models (Eistrup et al. 2016, 2018).

The first step in our compositional modeling is to determine the mass fraction of gas condensed as rock in the inner regions of the protoplanetary disk. In the framework of our study, it is not important whether this mass fraction initially condenses as dust, pebbles, or planetesimals, as long as planetesimals incorporate the bulk of it by the time the giant planet starts migrating. Comparing solar and meteoritic abundances and assuming that the rock-forming elements are condensed in meteoritic proportion (Lodders 2010; Palme et al. 2014), the

Table 1
Protosolar and Meteoritic Abundances of C, O, N, and S

Element	Protosolar Abundance	Meteoric Abundance	Protosolar/ Meteoritic Ratio
C	3.0×10^{-4}	2.6×10^{-5}	0.09
O	5.4×10^{-4}	2.6×10^{-4}	0.48
N	7.4×10^{-5}	1.9×10^{-6}	0.03
S	1.5×10^{-5}	1.5×10^{-5}	1.00

Note. Estimated abundances are expressed as relative abundances with respect to H atoms (Asplund et al. 2009; Lodders 2010).

mass fraction of disk gas condensing as rock is $Z_{\rm rock} = 6.6 \times 10^{-3}$ (see Figure 2 and Table 3).

By subtraction from the protostellar Z, the mass fraction of high-Z material that remains in the gas phase as volatiles, to progressively condense at larger distances as ices and organics, amounts to $Z_{\rm ice} = 7.5 \times 10^{-3}$. About 17% of $Z_{\rm ice}$ is provided by Ne, an element not included among our tracing elements but nevertheless contributing a significant fraction of the total high-Z material (see Asplund et al. 2009; Lodders 2010; Palme et al. 2014). Moreover, some molecules of the four elements we consider (specifically, CO and N_2) never condense in the protoplanetary disk, due to the adopted thermal profile. This means that the condensed fraction of high-Z elements across our template disk is always lower than the protostellar Z value, with $Z_{\rm ice} = 5.3 \times 10^{-3}$ representing the maximum mass fraction of condensed volatiles in the outer disk (see text below, as well as Figure 2 and Table 3).

The next steps involve distributing the four tracing elements across their carriers while preserving the mass balance. The protostellar and meteoritic abundances for the four tracing elements are reported in Table 1, together with their protostellar/meteoritic ratio; for details on the comparison methodology, see Asplund et al. (2009), Lodders (2010), and Palme et al. (2014). The distribution of the four tracing elements across the gas and solid phases is shown in Figure 3, while their partition among the different carriers (rocks, organics, ices) is reported in Table 2.

Based on meteoritic data for CI carbonaceous chondrites (Lodders 2010; Palme et al. 2014), chondritic rocky material carries the totality of S and about half the O, while it contains only 9% of C and 3% of N (see Figure 3 and Table 2). It is worth highlighting that chondritic rocks contain significantly more O than would be expected from a pure mixture of silicon, magnesium, and iron oxides (which would account only for ∼27% of the total O; see Lodders (2010) and Palme et al. (2014)), likely due to the presence of hydrated minerals (e.g., phyllosilicates) or refractory organic material (Pollack et al. 1994; Semenov et al. 2003).

The fractional abundance (48%) of O carried in refractory form in rocks determined above is consistent with the data on O fugacities of exoplanetary materials gathered from observations of polluted white dwarfs (Doyle et al. 2019). In parallel, the fractional abundance (100%) of S carried in refractory form in rocks determined from meteoritic data is consistent with the observations of the composition of material accreted by stars in a sample of young disk-hosting B–F stars (Kama et al. 2019). A comparison with the extrasolar data also reveals that the differences between the refractory/rocky component in our model (based on the protosolar composition) and analogous exoplanetary materials are on the order of ∼10%.

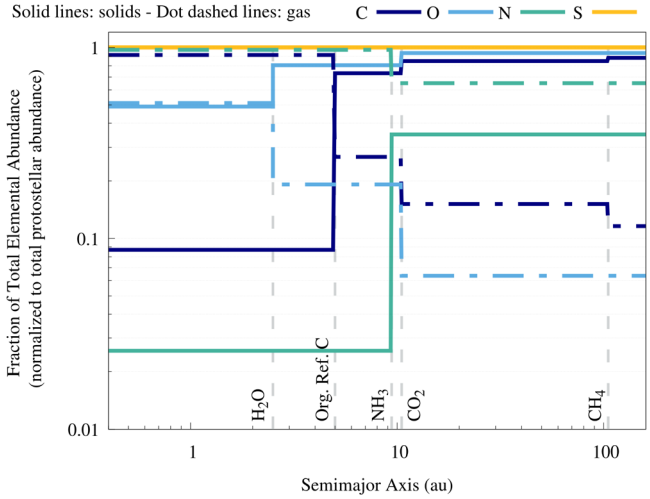

Figure 3. Fractions of C, O, N, and S in solid phase (solid lines) and gas phase (dotted–dashed lines) in the protoplanetary disk at varying distances from the host star. Values are normalized to the protostellar abundances reported in Tables 1 and 2. Vertical dashed lines indicate the position of the snowlines of H_2O (2.5 au), refractory organic carbon (5 au), NH_3 (9.4 au), CO_2 (10.5 au), and CH_4 (105 au).

Table 2
Protostellar Abundances and Partitioning of C, O, N, and S among Rocks, Organics, and Ices

Element	Protostellar Abundance	Partition among Phases		
		Rock	Refractory Organics	Ice
C	3.0×10^{-4}	2.6×10^{-5}	1.9×10^{-4}	8.0×10^{-5}
O	5.4×10^{-4}	2.6×10^{-4}	0	2.8×10^{-4}
N	7.4×10^{-5}	1.9×10^{-6}	0	7.2×10^{-5}
S	1.5×10^{-5}	1.5×10^{-5}	0	0

Note. Protostellar abundances of C, O, N, and S in our compositional model expressed as relative abundances with respect to H and their partitioning in condensed form between rocks, organics and ices. We refer readers to the main text for more details on the different solid phases and the adopted abundances.

The observations of the composition of comet 67P Churyumov–Gerasimenko (67P C–G in the following) by the ESA mission Rosetta provide further support for the leading role of refractory materials as the main carrier of S, in agreement with the results of Kama et al. (2019). Rosetta's observations show a relative abundance of H_2S, the main volatile carrier of S, of the order of 10^{-2} that of water (Le Roy et al. 2015; Rubin et al. 2019, 2020). In our compositional model, this amounts to ∼10% of the solar budget of S (see text below, as well as Table 2 and Figure 3). As a result, both cometary and extrasolar data constrain the accuracy of our partitioning of S to about 10%.

The majority of C and N, along with the remaining fraction (52%) of O not incorporated in rocks, are in the form of gas in the inner regions of the protoplanetary disks (see Figure 3). We took advantage of the astrochemical models from Eistrup et al. (2016, 2018) to determine how they partition across the different molecules and the different phases. Specifically, we used the abundances (rescaled as discussed below, to preserve mass balance) and condensation profiles of the different volatile molecules to estimate the abundances of C, O, and N atoms in the gas and condensed as ices as a function of the distance from the host star. Using the relevant molecular

Table 3
Condensation Sequence and Total Mass Fraction Z_i in Solid Phase across the Protoplanetary Disk

	Rocks	H_2O	Ref. Org. C	NH_3	CO_2	CH_4
Snow Line (au)	⋯	2.5	5.0	9.5	10.5	105
Z_i	6.6×10^{-3}	8.8×10^{-3}	1.04×10^{-2}	1.07×10^{-2}	1.18×10^{-2}	1.19×10^{-2}

Note. Cumulative mass fraction Z_i of all materials/molecules in solid phase across the different compositional regions of the protoplanetary disk due to the condensation of rocks, organics, and ices as illustrated in Figure 2. For each material/molecule in the condensation sequence (except rocks), we report the position of the associated snowline. Each value of Z_i represents the total mass fraction resulting from the whole condensation sequence up to the relevant snowline (e.g., the value at 9.5 au is due to the sum of rocks, H_2O, refractory organic C, and NH_3).

weights, we computed the mass contribution of each molecule of these elements to the condensed mass fraction Z_i (see Figure 2 and Table 3).

Among the evolutionary scenarios investigated by Eistrup et al. (2016, 2018), we focused on the one where the abundances of ices in planetesimals are inherited from the pre-stellar phase (labeled the "inheritance—low ionization" scenario in Eistrup et al. (2018)). This scenario was chosen based on the results of the comparison between Rosetta's observations of comet 67P C–G and the protostellar systems IRAS 16293-2422 and SVS13-A (Bianchi et al. 2019; Drozdovskaya et al. 2019), which suggest a significant imprint of interstellar chemical abundances on cometary ices (for a discussion, see also Altwegg et al. (2019)).

Our reference for the partitioning of C, O, and N among the different molecules is based on the results of the astrochemical models of Eistrup et al. (2018) after 1 Myr of evolution of the protoplanetary disk, for reasons we will discuss in the following. Before proceeding, it should be noted that the adopted disk chemical scenario is not unique: a discussion of the implications of different chemical scenarios for our analysis is provided in Section 4.4.

As shown in Figure 3, in the inheritance scenario from Eistrup et al. (2018), the bulk abundance of N is partitioned between NH_3 (∼33%) and N_2 (∼66%). Since the total abundance of N with respect to hydrogen ([N/H]) reported by Eistrup et al. (2016) (6.2×10^{-5}) is lower than the protostellar value derived from Asplund et al. (2009) and reported in Table 1, we scaled the total abundances of N, NH_3, and N_2 from Eistrup et al. (2016, 2018) by a common factor of 1.15. This ensures the conservation of the total mass of N in the protostellar disk, including the fraction incorporated in rocks (see Table 2), while preserving the chemical network and results of Eistrup et al. (2016, 2018).

In the case of O, the abundance of 5.2×10^{-4} reported for ices by Eistrup et al. (2016, 2018) is close to the protostellar abundance derived from Asplund et al. (2009) and reported in Table 1. This, however, neglects the amount of O sequestered in refractory form into chondritic rocks (see Figure 3 and Tables 1 and 2). We therefore scaled the abundance of O from Eistrup et al. (2016, 2018) by a factor of 0.57 to match the fraction of O in volatile form in our protoplanetary disk (see Table 2). Since O and C share a joint chemical network, we scaled the abundance of C of 1.8×10^{-4} from Eistrup et al. (2016, 2018) by the same factor of 0.57, to preserve the relative proportions of C- and O-bearing volatiles of their astrochemical models (see Table 2).

This scaling preserves the mass balance of O throughout the disk, but it leaves a fraction of C unaccounted for. However, previous work comparing the C/Si values observed in meteorites with those of interstellar dust (see Bergin et al. 2015, and references therein) highlighted the significant role played by carbonaceous dust and/or C-based organic compounds as reservoirs of solid C in planetary materials. The contribution of such reservoirs can account for ∼50% of the total carbon budget, exceeding that of rocks and C-based ices (Bergin et al. 2015), as recently supported by Rosetta's measurements of the C-rich composition of 67P C–G's dust (Bardyn et al. 2017; Isnard et al. 2019).

We followed Cridland et al. (2019) and previous authors (e.g., Thiabaud et al. 2014; Bergin et al. 2015; Mordasini et al. 2016) and included this additional C reservoir in our compositional model, alongside rocks and ices. In particular, following Cridland et al. (2019), we increased the amount of C in solid form included in planetesimals from 5 au outward to match the C/Si = 6 value observed in comet 67P C–G's dust (Bardyn et al. 2017) and in the interstellar medium (see Figures 2 and 3, as well as Table 3). This allows us to account for all missing C after the scaling described above. The transition at 5 au accounts for the destruction of carbonaceous dust in the inner regions of protoplanetary disks (Bergin et al. 2015). To preserve the C mass balance throughout the disk, the gas in the inner 5 au is proportionally enriched in C in the form of C–H bond molecules, as suggested by Rosetta's observations of the high H/C (≈1) ratio in 67P C–G's dust.

We adopt the naming convention from Thiabaud et al. (2014) and Isnard et al. (2019) and refer to this C reservoir as refractory organic C, in order to distinguish it from the C included in chondritic rocks (see Table 2). Before proceeding, it is important to note that the focus of our compositional model is on the distribution of the four tracing elements across the gas and solid phases in the disk (see Figure 3), not on the specific form in which the elements are incorporated into the planetesimals. Specifically, our model is not influenced by whether the additional C is incorporated as graphite, nanodiamonds, or C–H bond chains (a similar point is also valid for the incorporation of O in phyllosilicates or refractory organics).

Based on the abundances of the different volatile and organic carriers of C, O, and N discussed above, along with the results of the astrochemical models of Eistrup et al. (2016, 2018), we can compute how the mass fraction of condensed material grows throughout our template protoplanetary disk: the result and the associated compositional gradient are shown in Figure 2 and Table 3. As illustrated in Figures 2 and 3 and reported in Table 3, the snow lines of H_2O, NH_3, CO_2, and CH_4 are located at 2.5, 9.5, 10.5, and 105 au, respectively. Note that the total mass fraction of condensed material is always lower than the protostellar Z value, due to the missing contributions of CO and N_2, since they never condense in the thermal environment of our template disk, alongside that of Ne as discussed before.

It should be noted that our disk model assumes both thermal and compositional structures that are constant in time (see

Table 4
Formation Scenarios, Envelope Metallicity, and Compositions of the Giant Planets

Formation Scenario	Initial Core Position (au)	High-Z Elements Accreted			Total C	Total O	Total N	Total S
		Solids ($M_\oplus$)	Gas ($M_\oplus$)	Total ($M_\oplus$)				
1	5	2.2	2.1	4.3	2.8×10^{-4}	5.7×10^{-4}	7.6×10^{-5}	1.2×10^{-5}
2	12	3.9	1.6	5.5	4.0×10^{-4}	6.9×10^{-4}	8.1×10^{-5}	1.8×10^{-5}
3	19	6.3	1.4	7.7	5.3×10^{-4}	1.0×10^{-3}	1.0×10^{-4}	2.7×10^{-5}
4	50	13.6	1	14.6	9.7×10^{-4}	2.0×10^{-3}	1.4×10^{-4}	5.6×10^{-5}
5	100	19.5	0.9	20.4	1.4×10^{-3}	2.8×10^{-3}	1.8×10^{-4}	8.0×10^{-5}
6	130	31.8	0.8	32.6	2.2×10^{-3}	4.5×10^{-3}	2.7×10^{-4}	1.3×10^{-4}
Reference values (solar mixture)		...	...	4.3	3.0×10^{-4}	5.4×10^{-4}	7.4×10^{-5}	1.5×10^{-5}

Note. Formation scenarios considered in this work and resulting composition of the gaseous envelope of the giant planet. For each scenario, we report the initial position of the giant planet, the accreted mass of high-Z elements due to planetesimals and gas as well as the total one due to both contributions, and the final abundances with respect to H of C, O, N, and S in the gaseous envelope. For reference, at the bottom of the table, we also report the values the gaseous envelope would possess if it were characterized by a purely solar composition. Note how, in scenario 1, the quantity of high-Z elements matches the solar one, yet O and N are super-solar while C and S are sub-solar.

Equation (8) and Figures 2 and 3). In evolving protoplanetary disks, however, the positions of the snowlines will drift inward over time in response to the evolving disk environment, which will affect its compositional structure (Eistrup et al. 2018, and references therein).

Recent comparisons between the masses of exoplanetary systems and of the dust and gas in protoplanetary disks suggest that the bulk of the planetesimal formation process should occur rapidly on a timescale of 1 Myr over the whole disk (Manara et al. 2018), which is consistent with meteoritic data from the Solar System (e.g., Scott 2007). The conversion of dust into planetesimals should cause gas-grain chemistry to become increasingly less efficient and the chemical evolution of the disk to slow down with respect to what would be expected in a dust-rich environment.

As a consequence, once most of the mass initially present as dust is converted into planetesimals, the compositional structure of the protoplanetary and planetesimal disks can be reasonably approximated as fixed. As discussed above, and consistent with the timescale reported by Manara et al. (2018), we adopted the results of the astrochemical models of Eistrup et al. (2018) after 1 Myr of evolution of the protoplanetary disk as our reference. The implications of temporally evolving disk models will be considered in future works. We refer the readers to Section 4 for further discussion of this issue.

3. Results

As introduced in Section 2, we investigated a set of six formation and migration scenarios, each with the seeds of the giant planet starting their growth and migration at different distances from their host star. As summarized in Table 4, the initial semimajor axes of the giant planet we considered were 5, 12, 19, 50, 100, and 130 au, respectively, with the giant planet concluding its migration at 0.4 au in all scenarios. In each simulation, we recorded the flux of impacts between the dynamical tracers representing the planetesimals and the giant planets, from which we then computed the total accreted mass of solid material as detailed in Section 2.4.

Using the compositional model described in Section 2.5, we then converted the accreted masses of gas and planetesimals into the total mass of accreted high-Z elements and the atomic abundances of C, O, N, and S with respect to H in the gaseous envelope of the giant planet. As discussed in Section 2.4, high-Z elements are assumed to be uniformly distributed in the gaseous envelope. The outcomes of our simulations are shown in Tables 4 and 5. Since our compositional model focuses on host stars that are solar analogs, in the following we will refer to solar abundances and stellar abundances interchangeably.

Table 5
Gas Contributions to the C, O, and N Abundances of the Gaseous Envelope

Formation Scenario	Gas Contribution		
	C	O	N
1	2.5×10^{-4}	2.3×10^{-4}	7.4×10^{-5}
2	1.8×10^{-4}	1.5×10^{-4}	7.1×10^{-5}
3	1.4×10^{-4}	1.2×10^{-4}	6.6×10^{-5}
4	7.6×10^{-5}	6.5×10^{-5}	5.5×10^{-5}
5	5.7×10^{-5}	4.7×10^{-5}	5.2×10^{-5}
6	5.3×10^{-5}	4.3×10^{-5}	5.1×10^{-5}
Solar	3.0×10^{-4}	5.4×10^{-4}	7.4×10^{-5}

Note. Gas contributions to the C, O, and N abundances in the gaseous envelope of the giant planet for the scenarios reported in Table 4. At the bottom of the table, we also report the respective contributions of an equivalent amount of gas with solar composition.

3.1. Planetesimal Accretion, Orbital Migration, and Planetary Metallicity

A first, immediate result shown by Table 4 is the direct correlation between the extent of migration and the enrichment of the giant planet due to the accretion of planetesimals: the larger the migration, the greater the enrichment. This result is in line with the findings of the work by Shibata et al. (2020), where they investigated the enrichment in heavy elements by migrating giant planets in disks more compact and more massive than the one we considered in our work. The range of total envelope metallicities reported in Table 4 spans the whole 1σ uncertainty range in the mass–metallicity trend of Jovian planets from Wakeford et al. (2017) and Sing (2018) based on Solar System and exoplanetary data (see also Table 6).

As can be seen in Table 4, the metallicity of the gaseous envelope is well-approximated by the accreted mass of planetesimals when giant planets undergo extensive migration (scenarios 4–6). However, in the case of moderate migration, the two quantities become increasingly different due to the

Table 6
Elemental Ratios and Metallicity of the Gaseous Envelope

Formation Scenario	Gas + Solids					Gas Only			
	Z	C/O	N/O	C/N	S/N	Z	C/O	N/O	C/N
1	1.0	0.49	0.13	3.64	0.16	0.5	1.13	0.33	3.43
2	1.3	0.58	0.12	4.95	0.22	0.4	1.24	0.48	2.57
3	1.8	0.53	0.10	5.31	0.27	0.3	1.15	0.56	2.07
4	3.4	0.50	0.07	6.80	0.39	0.2	1.18	0.86	1.38
5	4.8	0.50	0.07	7.54	0.44	0.2	1.22	1.10	1.11
6	7.6	0.50	0.06	8.28	0.48	0.2	1.22	1.18	1.04
Solar	1.0	0.55	0.14	3.98	0.20	1.0	0.55	0.14	3.98

Note. Elemental ratios and metallicity Z (in units of solar metallicity) of the gaseous envelope of the giant planet in the different formation scenarios when considering the contributions of both gas and solids and that of gas only. At the bottom of the table, we report the respective solar elemental ratios, for comparison. The metallicity Z in the gas and solids case is computed from the total accreted high-Z material in Table 2, while in the gas-only case it is computed from the gas-accreted high-Z material reported in the same table.

growing contribution from the accreted gas (scenarios 1–3; see also Table 5). The transition between the two regimes will depend on the extension and metallicity of the host protoplanetary disk. Extrapolating from the trend in Table 4, in the case of limited migration, the final metallicity of the planetary envelope can be sub-stellar, in line with the findings by Turrini et al. (2015) and references therein, as well as those of Shibata & Ikoma (2019) and Shibata et al. (2020).

Once considered together, our results and those of Shibata et al. (2020) support the view that giant planets characterized by super-stellar metallicity values should have formed at markedly larger distances from their host stars than their counterparts characterized by sub-stellar metallicity values, unless the latter formed via a different mechanism (e.g., by disk instability). In the case of large protoplanetary disks like that considered in this work, our results indicate that super-stellar metallicity values require formation regions consistent with those of the giant planets indirectly identified by ALMA's observational surveys (e.g., ALMA Partnership et al. 2015; Isella et al. 2016; Fedele et al. 2017, 2018; Andrews et al. 2018; Long et al. 2018).

When the atomic abundances of C, O, N, and S with respect to H are computed from the accreted masses of gas and planetesimals, the results reported in Table 4 also show how the final planetary composition is markedly non-solar/non-stellar and highlight the lack of simple and common relationships between metallicity and atomic elemental abundances. An immediate example is provided by scenario 1, where the giant planet starts to form at 5 au: the metallicity is solar, but O and N are super-solar while C and S are sub-solar.

3.2. C/O Ratios of Gas-dominated and Solid-enriched Giant Planets

The next step in our analysis has been to compute the overall C/O ratios of the giant planets at the end of the simulations. For comparison, we also computed the C/O ratios that the same giant planets would have solely due to the gas they accreted, ignoring the contribution of the captured planetesimals. This second set of values can be physically interpreted as the C/O ratio of late-formed giant planets that migrated through protoplanetary disks already depleted of planetesimals by the passage of early-formed giant planets or by their radial drift induced by gas drag (e.g., Turrini et al. 2015).

In the following, we will refer to solid-enriched giant planets when considering the contributions of both gas and solids, and to gas-dominated giant planets when considering only the contribution of gas. In the latter case, we will focus on elemental ratios involving only C, O, and N, as S is supplied only by planetesimals. Both sets of C/O ratios are reported in Table 6 and shown in the top panel of Figure 4, where it is immediately evident that different and somewhat opposite behaviors characterize them.

The C/O ratios of gas-dominated giant planets are markedly super-stellar and always have values greater than unity (see the green line and circle symbols in the top panel of Figure 4). Conversely, the values of the C/O ratios of solid-enriched giant planets are close to the solar value and predominantly sub-solar (see the purple line and square symbols in the top panel of Figure 4). These behaviors are a direct consequence of the distribution of C and O throughout the protoplanetary disk, and particularly due to the fact that the bulk of O and C gets trapped into solids within the first 2–5 au from the host star through rocks, H_2O ice, and refractory organic C (see Figures 2 and 3 and Section 2.5).

The effects of this early trapping of the bulk of C and O in solids are illustrated by the bottom panel of Figure 4, which shows the C/O ratios of the gas (green dotted–dashed line) and solids (purple solid line) in the protoplanetary disk. Like the snowline of H_2O, the snowlines of refractory organic C and CO_2 are an order of magnitude closer to the star than that of CH_4: as a consequence, across most of the disk extension, the C/O of the solids is characterized by slightly sub-solar values. In contrast, the C/O ratio of the gas is characterized by values around one, i.e., roughly twice the solar value.

As a result of the balance between accreted gas and solids (see Table 4), the C/O ratio of solid-enriched giant planets starting their formation beyond the CO_2 snowline (scenarios 3–6) monotonically decreases for increasing initial distances from the host star (or equivalently, for increasing migration). Still, this variation is extremely limited (about 10%; see Figure 4). A similar yet opposite monotonic behavior occurs for gas-dominated giant planets: their C/O ratios increase (also by about 10%; see Figure 4) for increasing initial distances from the star.

Both monotonic behaviors described above break once the giant planets start their formation close to or inside the CO_2 snowline (scenarios 1 and 2). Both solid-enriched and gas-dominated giant planets show a peak in their C/O ratio in

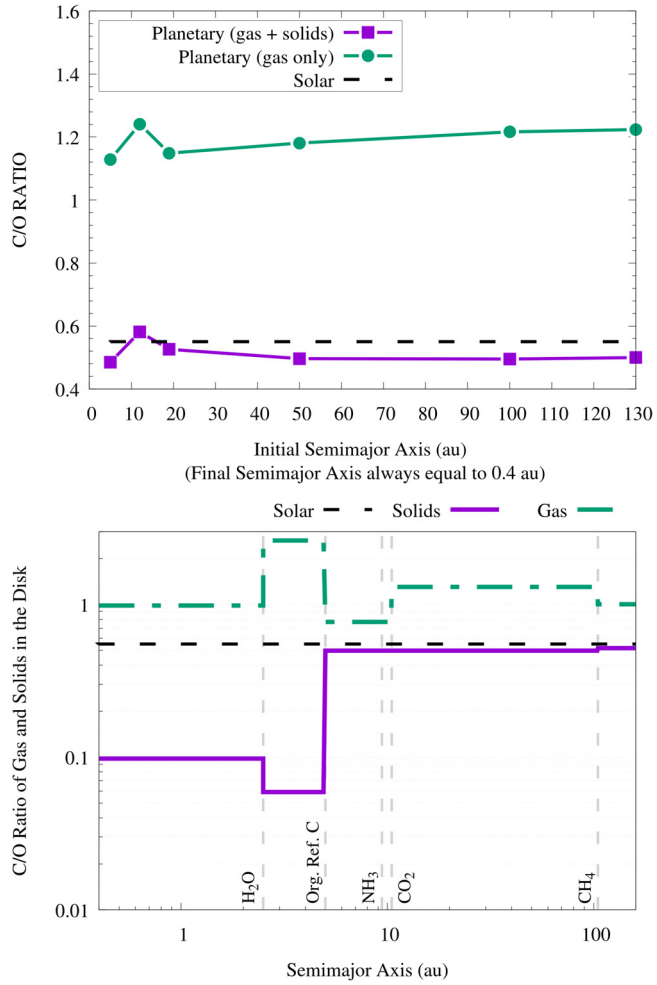

Figure 4. Top: Final C/O ratios of the gaseous envelope of the giant planet as a function of its initial orbital position for the cases of solid-enriched giant planets (purple line and squares) and gas-dominated giant planets (green line and circles). Bottom: C/O ratios of the gas (green dotted–dashed line) and the solids (purple solid line) throughout the protoplanetary disk. Dashed lines show the stellar C/O ratio, which is the same as the solar one. We refer the readers to Section 3.2 for details.

scenario 2 (giant planet starting to form at 12 au) due to a large amount of C-rich gas accreted between the snowlines of refractory organic C and H_2O (see Figure 4, bottom panel). The C/O ratio then decreases again for giant planets starting to form within the NH_3 snowline.

Overall, our results suggest a dichotomy in the C/O ratio when giant planets form at large distances from their host stars, with values above one for gas-dominated giant planets and about stellar for the solid-enriched ones. The fact that, for both classes of planets, the C/O ratio never varies by more than 10% between different migration scenarios also suggests that, depending on the characteristics of the native protoplanetary disk, the diagnostic power of the C/O ratio might be limited. Specifically, it might not allow for distinction between giant planets that formed closer to or farther from their stars, instead distinguishing only between gas-dominated or solid-enriched giant planets.

3.3. Planetary Migration and the C/N and N/O Ratios

Due to the possible limitations of the C/O ratio with regard to discriminating between different formation regions and migration histories, we focused our attention on two ratios involving N, the third-most abundant element among those we considered. Specifically, we considered the C/N and the N/O ratios. Their behavior is shown in Table 6 and Figure 5, where we again consider the cases of solid-enriched and gas-dominated giant planets as discussed in Section 3.2.

The C/N ratio of solid-enriched giant planets grows monotonically from a value of 3.6 in scenario 1 to a value of 8.3 in scenario 6 (see Table 6), i.e., it grows with migration by about a factor of two. The C/N ratio of gas-dominated giant planets is characterized by the opposite trend. It grows smaller with migration by a factor of three, monotonically decreasing from a value of 3.4 in scenario 1 down to one in scenario 6.

The N/O ratio shows a similar but inverse behavior: the N/O ratio of solid-enriched giant planets decreases monotonically with migration. In contrast, the N/O ratio of gas-dominated giant planets increases monotonically. In the case of gas-dominated giant planets, the N/O ratio goes from a value of 0.3 in scenario 1 to a value of 1.2 in scenario 6, i.e., it grows by about a factor of four. For solid-enriched giant planets, the N/O ratio varies instead from a slightly sub-solar value of 0.13 in scenario 1 to about 0.06 in scenario 6, i.e., it decreases by a factor of two.

It should be pointed out that the range of values discussed above is model-dependent, even if the overall behavior of the two ratios is not. The specific values of the C/N and N/O ratios depend on the partitioning of C, O, and N among the different snowlines (see Figure 3). As a result, the slope of the curves and the value of the C/N and N/O ratios will vary with the chemical and thermal profiles of protoplanetary disks. We will further explore this dependence in Section 4.2.

Nevertheless, the trends discussed above depend exclusively on the fact that the bulk of N in disks is in the form of N_2 and that the N_2 snowline is farther away from the host star than all the C and O snowlines (see Figure 3). While these two conditions are satisfied, the amount of C and O sequestered in solids will increase with the orbital distance faster than the amount of N, resulting in C/N and N/O trends similar to those shown in Figure 5.

The larger the deviation of the C/N and N/O ratios from the stellar values, therefore, the larger the orbital distance crossed by the giant planet during its disk-driven migration. Moreover, while the C/N ratio of both gas-dominated and solid-enriched giant planets might be observationally indistinguishable from the stellar one in the case of giant planets that experienced limited migration (see scenario 1 in the left-hand panel of Figure 5), the same does not apply to the N/O ratio.

A fraction of O varying between a quarter and half of its total abundance is already incorporated into rocks in the innermost regions of protoplanetary disks (Lodders 2010; Palme et al. 2014; Doyle et al. 2019); see Figure 3 and Section 2.5 for further discussion. Consequently, the N/O ratio of gas-dominated giant planets will always be characterized by super-solar values (see scenario 1 in the right-hand panel of Figure 5).

More generally, the comparison between Figures 4 and 5 highlights how the joint use of the three elemental ratios, C/O, C/N, and N/O, allows us to more easily break possible degeneracies in the interpretation of their values and their link with the formation and migration history of giant planets.

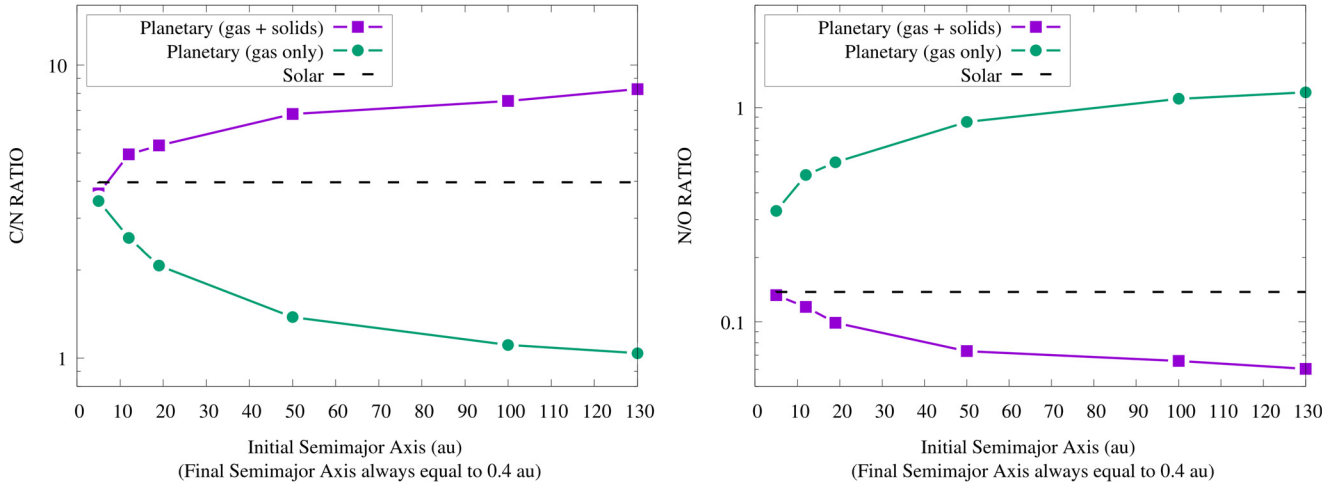

Figure 5. C/N (left) and N/O (right) ratios of the gaseous envelope of the giant planet as a function of its initial orbital position. In the figure, we show the cases of solid-enriched giant planets (purple line and squares) and gas-dominated giant planets (green line and circles). Dashed lines show the stellar C/N and N/O ratios, which are the same as the solar ones. We refer the readers to Section 3.3 for details.

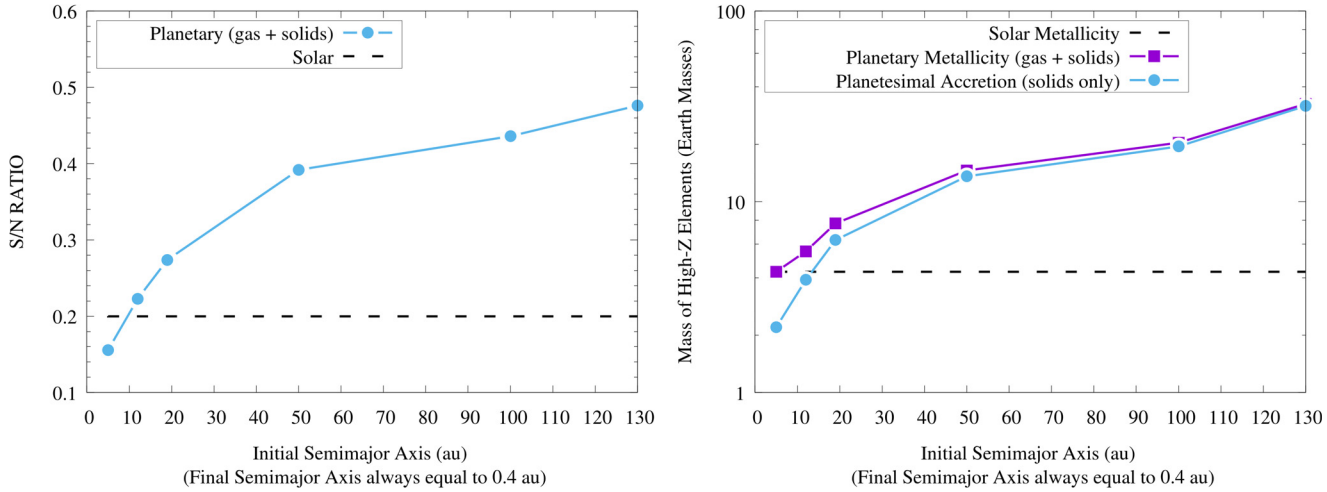

Figure 6. S/N ratio (left), metallicity, and mass of accreted planetesimals (right) of solid-enriched giant planets as a function of their initial orbital positions. Dashed lines show the stellar S/N ratio and the mass of high-Z elements equivalent to the stellar metallicity, which are the same as the solar ones. We refer the readers to Section 3.4 for details.

3.4. Planetesimal Enrichment and the S/N Ratio

The final focus of our analysis has been the investigation of the S/N ratio as a direct tracer of the enrichment in heavy elements of giant planets. As highlighted by our results (see Section 3.1, as well as Tables 4 and 5), both the metallicity and the composition of the gaseous envelope of giant planets are strongly affected by the enrichment in high-Z elements due to planetesimal accretion.

The planetary metallicity, however, coincides with the enrichment due to planetesimal accretion only in the case of extensive migration of the giant planet. In contrast, in cases of moderate or limited migration, the two quantities increasingly diverge (see Table 4, as well as the comparison between the purple and blue lines in the right-hand panel of Figure 6). The planetary metallicity, moreover, is constrained indirectly through the planetary mass–radius relationship, and as such, its estimation is affected by the uncertainties not only on the measurements of both quantities but also on the interior modeling of giant planets.

The investigation of the formation and migration histories of giant planets through their envelope metallicity would therefore benefit from additional and independent constraints on the enrichment in heavy elements due to planetesimal accretion. As shown by Figure 6 and Tables 4 and 6, the S/N ratio provides such an independent constraint, as its value monotonically grows with migration (Figure 6, left-hand panel) and is proportional to the mass of accreted planetesimals (see the blue curves in the left- and right-hand panels of Figure 6).

The proportionality between S/N and enrichment is not linear, as illustrated by the different scales of the S/N and planetesimal accretion curves as a function of migration (linear for the S/N values in the left-hand panel, logarithmic for the planetesimal accretion in the right-hand panel of Figure 6). This difference is a reflection of S representing a decreasing fraction per unit mass of the planetesimals for increasing distances from the host star.

Specifically, inside the H_2O snowline, planetesimals are composed of chondritic rock (see Figure 2), which is the main carrier of S (see Figure 3 and Section 2.5). Moving away from the star, the composition of planetesimals will include increasing contributions of volatile materials (H_2O, CO_2, NH_3, etc.; see Figure 2) not traced by S. As can be seen from

Table 7
Normalized Elemental Ratios of the Gaseous Envelope

Formation Scenario	Gas + Solids				Gas Only		
	C/O^*	N/O^*	C/N^*	S/N^*	C/O^*	N/O^*	C/N^*
1	0.88	0.97	0.91	0.80	2.05	2.38	0.86
2	1.06	0.85	1.24	1.14	2.26	3.50	0.65
3	0.96	0.72	1.33	1.40	2.09	4.02	0.52
4	0.90	0.53	1.71	2.00	2.15	6.20	0.35
5	0.90	0.48	1.89	2.23	2.21	7.94	0.28
6	0.91	0.44	2.08	2.44	2.23	8.52	0.26

Note. Elemental ratios of the gaseous envelope of the giant planet normalized to the respective stellar values in the different formation scenarios when considering the contributions of both gas and solids and of gas only. A value of 1 indicates a stellar value of the elemental ratio.

Figure 2, in the outer regions of the disk, S will trace only half the mass (i.e., the rocky fraction) accreted through planetesimals. Consequently, while the proportionality coefficient between S/N and planetesimal accretion is constant within any given pair of snowlines (i.e., for a constant planetesimal composition), it changes each time a snowline is crossed (see Figures 2 and 6).

Nevertheless, the behavior of the S/N ratio as a tracer of the enrichment from planetesimal accretion shown in Figure 6 depends only on the fact that, while the bulk of N in disks is in gaseous form as N_2 (see Figure 3 and Section 2.5, as well as Eistrup et al. (2016, 2018), Bosman et al. (2019), and Öberg & Wordsworth (2019)), the bulk of S is instead trapped in refractory solids (see Figure 3 and Section 2.5, as well as Lodders (2010), Palme et al. (2014), and Kama et al. (2019)). Consequently, even if the slope of the S/N curve as a function of planetary migration will depend on the NH_3–N_2 and the S refractory-volatile partitionings, the direct proportionality between S/N ratio, planetary migration and enrichment in high-Z elements due to planetesimal accretion will not.

A close match between the planetesimal enrichment estimated through the S/N ratio and independent evaluations of the planetary metallicity, therefore, provides a strong indication that the giant planet under investigation formed at large distances from the host star and underwent extensive disk-driven migration. Conversely, a sub-stellar S/N ratio coupled with an estimated stellar or super-stellar planetary metallicity provides a clear indication that the giant planet experienced a moderate disk-driven migration and its metallicity is due to the joint contributions of gas and planetesimals.

4. Discussion

Our results show how the C/N, N/O, and S/N ratios can be used as tracers of migration and planetary metallicity in studying the formation and dynamical history of individual giant planets, complementing the information provided by the C/O ratio. The different ranges of values they span, however, can hinder the efficient joint use of the four elemental ratios.

Moreover, the specific shapes of the curves of the four elemental ratios discussed in Section 3 depend on the characteristics of the host system and the thermochemical environment of its protoplanetary disk. For the tracers we investigated, the partitioning of N between NH_3 and N_2 is particularly critical, as it determines the amount of N accreted with solids—and, consequently, the slope of the C/N, N/O, and S/N curves.

In the following, we will show how the use of elemental ratios normalized to the respective stellar values allows for extracting information from the composition of giant planets and drawing general conclusions on their formation history, even in the absence of detailed information regarding their birth environment. To further test the validity of these normalized ratios, we will also investigate a compositional scenario characterized by an alternative NH_3:N_2 partitioning with respect to that of Eistrup et al. (2016, 2018), shown in Figure 3.

4.1. Normalized Elemental Ratios and Their Joint Use

To address the obstacle posed by the different ranges of values spanned by C/O, C/N, N/O, and S/N, we investigated the use of normalized ratios, where each ratio is expressed in units of the corresponding stellar value. In this scale, giant planets whose composition matches that of their host stars will possess C/N, N/O, and S/N ratios all equal to unity.

We recomputed the elemental ratios discussed in Section 3 in this normalized scale: the normalized ratios are reported in Table 7 while their resulting trends are shown in Figure 7, where we separate between gas-dominated (right-hand panel) and solid-enriched giant planets (left-hand panel). To avoid confusion between the normalized and non-normalized ratios, in the following we will refer to the normalized ratios as C/O^*, N/O^*, C/N^*, and S/N^*.

The direct benefit of this normalization is that the curves associated with the different elemental ratios can be more easily plotted together and compared. Their comparison immediately highlights additional information provided by the joint use of the C/O^*, C/N^*, and N/O^* ratios. For gas-dominated giant planets, N/O^* will be greater than C/O^*, which will in turn be greater than C/N^* (see Figure 7, left plot, as well as Table 7).

For solid-enriched giant planets, the situation is inverted and C/N^* will be greater than C/O^*, which will in turn be greater than N/O^* (see Figure 7, right plot, as well as Table 7). In both cases, the separation between the values of the three normalized ratios will increase with the extent of disk-driven migration experienced by the giant planet. In other words, the farther from the star a giant planet will start its formation, the more significant the difference between its C/N^*, C/O^*, and N/O^* ratios.

The inclusion of the S/N^* ratio in the comparison provides a further piece of information. Giant planets that experienced limited migration and enrichment in solid material will have C/N^* ratios higher than the S/N^* ratios (see Figure 7). This is a result of the comparatively large C contribution of the accreted gas, while S is supplied only by the limited amount of captured solids. Giant planets that experienced a significant migration and whose metallicity is dominated by the accretion of

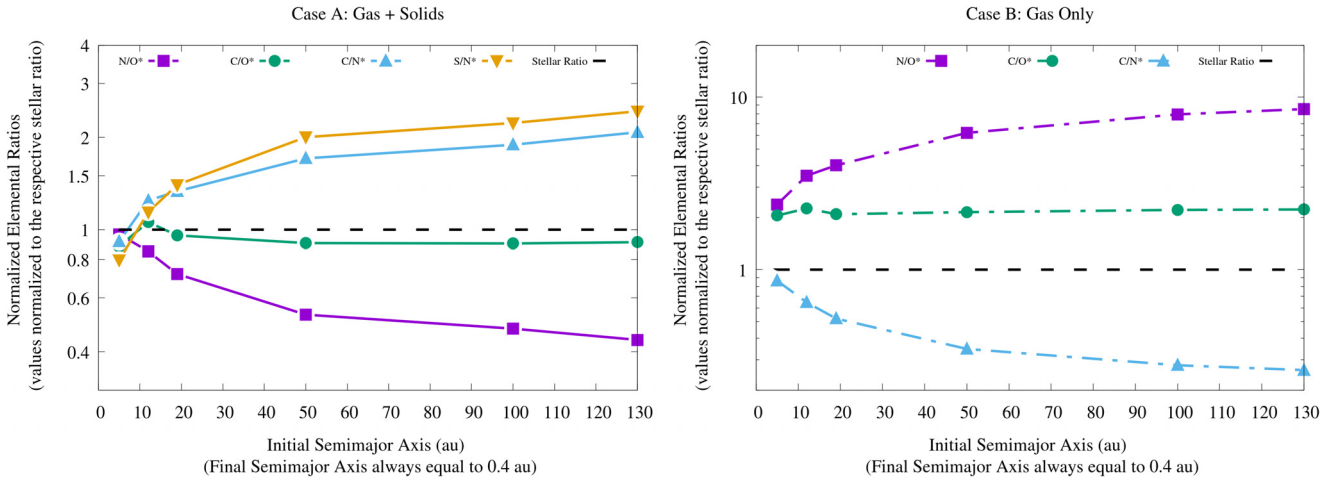

Figure 7. Left: Normalized elemental ratios of the gaseous envelope when the metallicity of the giant planet is dominated by the accretion of planetesimals. Right: Normalized elemental ratios in the gaseous envelope when the metallicity of the giant planet is dominated instead by the accretion of gas. Each elemental ratio is normalized to the relevant stellar elemental ratio.

planetesimals will have S/N^* ratios higher than the C/N^* ratios (see Figure 7), as the gas cannot compensate for the lower accretion of C with respect to S with solids.

It is important to highlight how the relative behavior of the elemental ratios described above and shown in Figure 7 is not an exclusive outcome of our compositional model. It is the general and direct result of the fact that, in protoplanetary disks, the bulk of S is incorporated in solids before the bulk of O and C, which in turn are incorporated into solids before the bulk of N. Furthermore, it is important to highlight that the role played by S in constraining the contribution of planetesimal accretion to the metallicity of giant planets is not unique to this element. As shown by Turrini et al. (2018), any element whose main carrier is characterized by a volatility similar to or lower than that of S (or more generally, O and C) can be used to the same effect.

Consequently, the relative contributions of gas and planetesimals to the metallicity can be constrained by comparing the C/N^* ratio with the normalized relative abundances with respect to N of rock-forming elements (e.g., Fe/N^*, Si/N^*, Mg/N^*), refractory elements (e.g., Ti/N^*, Ca/N^*, Al/N^*), or moderately volatile elements (e.g., Cl/N^*, Cr/N^*, Na/N^*), as all these elements will be characterized by similar enrichment patterns. For further discussion, see Turrini et al. (2018), as well as Lodders (2010), Palme et al. (2014), and Palme & Zipfel (2017) for the observational and meteoritic perspective, in addition to Kama et al. (2019) for the specific case of Ti.

4.2. Implications of the NH_3:N_2 Ratio in the Disk

The partitioning of N between NH_3 and N_2 plays a central role in determining the N-based elemental ratios under investigation, both in their standard and normalized forms. The higher the fraction of N that remains in gaseous form as N_2, the steeper the slopes of the curves of the N-based elemental ratios. Recent work (Bosman et al. 2019) argued that the 1:1 NH_3:N_2 ratio adopted by astrochemical models of protoplanetary disks (Eistrup et al. 2016, 2018) should be considered as an upper limit, and based on observational data, realistic partitioning should include significantly less ammonia.

To explore the impact of a lower abundance of NH_3 in protoplanetary disks, we modified our compositional model by changing the NH_3:N_2 ratio. We considered an alternative scenario where the NH_3:N_2 ratio is 2:9, which is equivalent to assuming that 90% of N is in the form of N_2 and only 10% is in the form of NH_3 (the major source of solid N in our compositional model). This alternative scenario falls into the range of values discussed by Öberg & Wordsworth (2019) and Bosman et al. (2019), and is consistent with the total N abundances measured by Rosetta in the dust and ices of comet 67P C–G (see Rubin et al. 2019, and references therein). The rest of the compositional model is kept unaltered. The normalized elemental ratios computed in this alternative compositional scenario are shown in Figure 8.

The only change between the alternative and standard compositional scenarios is in the slopes of the curves of the N-based elemental ratios. A comparison of Figures 7 and 8 reveals that the change is more marked in the case of solid-enriched giant planets, whose C/N^* and S/N^* ratios reach values twice as large as those in the standard scenario for large-scale migration. Similarly, the N/O^* ratio reaches values half as large as those in the standard scenario. Analogous but more subdued changes are seen for gas-dominated giant planets, where the N/O^* (C/N^*) ratio increases (decreases) by ∼30%.

Overall, the comparison between the alternative and standard compositional scenarios shows that the global picture and the trends discussed in Sections 3 and 4.1 do not depend on a specific partitioning of N among NH_3 and N_2; instead, they rely solely on the fact that the bulk of N remains in gaseous form as N_2 for most of the extension of protoplanetary disks and condenses as ice farther away from the star than S, O, and C.

The use of N-based elemental ratios as chemical tracers of the formation history of giant planets actually benefits from abundances of NH_3 in protoplanetary disks lower than those assumed in our standard compositional model. Lower NH_3 abundances enhance the contrast in the C/N^* and N/O^* ratios between different migration scenarios, allowing more accurate constraints to be placed on the formation regions and migration tracks of giant planets.

4.3. Observational Determination of the Elemental Ratios

Our focus in this work has been on investigating the information content provided by the different elemental ratios on the formation history of giant planets. Such elemental ratios need to be retrieved from the atmospheric abundances of the

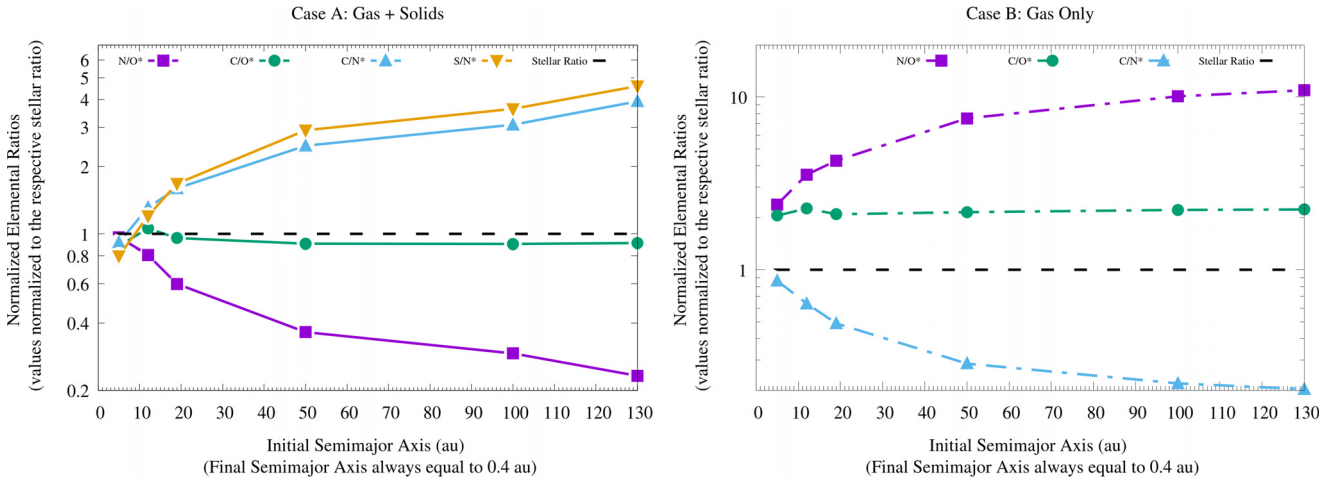

Figure 8. Same as Figure 7 but assuming a 9:2 N_2:NH_3 ratio instead of the 1:1 ratio from Eistrup et al. (2016, 2018) adopted in our standard compositional model. The contrast among the different elemental ratios in the solid-enriched metallicity case is enhanced by a factor of two, while the effects of this alternative partitioning are more limited in the gas-dominated metallicity case.

main molecular carriers of C, O, N, and S by means of spectral observations; for further discussion, see Madhusudhan et al. (2016), Madhusudhan (2019), and references therein. Such observations will be systematically performed by the JWST (Cowan et al. 2015; Greene et al. 2016) and Twinkle (Edwards et al. 2018), and will be the main goal of the Ariel mission (Tinetti et al. 2018).

The specific molecular carriers of C, O, N, and S in an exoplanetary atmosphere will depend on its temperature and metallicity and on whether the atmospheric chemistry is governed by chemical equilibrium or disequilibrium (e.g., Madhusudhan et al. 2016; Venot et al. 2018; Madhusudhan 2019; Drummond et al. 2020, and references therein). With regard to S, the main molecular carrier is expected to be H_2S over a wide range of atmospheric temperatures (Fegley & Schaefer 2010; Woitke et al. 2018). Under the assumption of chemical equilibrium, the main molecular carriers of C and O are expected to be H_2O and CH_4 for atmospheres colder than about 1200 K at the pressure of 1 bar and H_2O, CO, and CO_2 for hotter ones (e.g., Fegley & Schaefer 2010; Madhusudhan et al. 2016).

Similarly, the main carriers of N are expected to be NH_3 for atmospheres colder than about 700 K at the pressure of 1 bar and N_2 for hotter ones (Fegley & Schaefer 2010; Madhusudhan et al. 2016). N_2 represents only a source of atmospheric opacity, but it cannot be identified directly by means of spectral observations, which would make the retrieval of the atmospheric abundance of N impossible for exoplanets hotter than 700 K. However, MacDonald & Madhusudhan (2017a, 2017b) reported the detection of NH_3 and HCN in the atmospheres of hot Jupiters, suggesting an important role of disequilibrium chemistry (see also Venot et al. 2018) and the possibility to retrieve the abundance of N also at higher temperatures. Other studies also found potential evidence for those molecules in planets such as HAT-P-38 b (Fisher & Heng 2018; Tsiaras et al. 2018) or HD-3167c (Guilluy et al. 2021). However, those detections are very challenging with the Hubble Space Telescope, as the molecular signals can be easily masked by water vapor and can be model-dependent (Pinhas et al. 2018; Changeat et al. 2020).

The atmospheric abundances of all these molecular species can be effectively retrieved with the JWST (MacDonald & Madhusudhan 2017a, 2017b; Min et al. 2020) and Ariel (Tinetti et al. 2018; Changeat et al. 2020; Min et al. 2020) telescopes. In the specific case of Ariel, moreover, Changeat et al. (2020) have recently shown that the abundances of H_2O, CO, CO_2, CH_4, and NH_3 can be retrieved even in cases of markedly sub-solar abundances. While the observational implications of our results will be the subject of future dedicated investigations, retrieving the atmospheric abundances of H_2O, CO, CO_2, CH_4, NH_3, HCN, and H_2S should allow us to directly estimate the elemental ratios discussed in this work and constrain the formation history of giant planets.

4.4. Caveats and Limitations on Modeling and Results

Our modeling of the formation history of giant planets and of its compositional implications aims to capture the essential aspects of this complex process, and both the thermal and compositional structures of the protoplanetary disk in this work are based on Solar System data cross-calibrated with a number of extrasolar sources. As already reported in Section 2, however, there are underlying assumptions and approximations that will require future investigations. We provide a brief discussion of their implications in the following.

4.4.1. Characterization of the Protoplanetary Disk Environment

Our model of the protoplanetary disk is a static one where both the thermal and the compositional structures are assumed as frozen over time. From a physical point of view, this approximation can be viewed as equivalent to assuming that the conversion of dust and pebbles into planetesimals occurs rapidly on a timescale that is shorter than that over which the protoplanetary disk evolves chemically. The sequestration of the bulk of the solid mass into planetesimals would cause the solid–gas interactions (e.g., gas-grain chemistry, condensation, and desorption of ices) to become less effective due to the less favorable surface-to-volume ratio of planetesimals with respect to dust, slowing down the chemical evolution of the disk. This approximation is not unreasonable, based on the short timescales over which dust appears to be converted into planetesimals in disks (e.g., Scott 2007; Manara et al. 2018, and references therein) and the comparisons of the volatile budgets of comets and protostellar systems (e.g., Bianchi et al. 2019;

Drozdovskaya et al. 2019), but it represents only one possible scenario.

Protoplanetary disks are expected to evolve over time both in terms of their temperature profile and their distribution of the solid materials with respect to the gas. The cooling of the disk over time will result in an inward drift of the snowlines (e.g., Panić & Min 2017; Eistrup et al. 2018), while the coupled interactions between radially drifting pebbles and dust grains and the thermal structure of the disk can result in the enrichment in heavy elements of the gas inward to the different snowlines due to the sublimation of the ices that cross the latter (Piso et al. 2016; Booth & Ilee 2019; Bosman et al. 2019).

While the implications of evolving disk environments on the compositional tracers discussed here will be addressed in future works, in the adopted compositional model, the bulk of S, C, and O are incorporated into low-volatility phases as refractories, organics, and water ice. In parallel, the most volatile ices CO and N_2 never condense, while CH_4 accounts for a minimal part of the C and mass budgets (see Figures 2 and 3). The only ice abundant enough in our compositional model to affect the chemical structure of the disk would be CO_2 (see Figures 2 and 3). The inner location of its snowline, however, would cause the effects of CO_2 sublimation to be limited for giant planets accreting most of their mass at larger distances from the star.

The sublimation-driven enrichment of heavy elements of the disk gas described by Piso et al. (2016) and Booth & Ilee (2019) is, therefore, going to be less pronounced in our template disk than in colder, more ice-rich disk scenarios (Bosman et al. 2019), and should not have a marked effect on the results we described. Moreover, as discussed in Section 4.1, the comparison between the C/N^* and S/N^* ratios would allow us to constrain the relative contributions of gas and planetesimals to the planetary metallicity. The possibility of discerning giant planets whose metallicity is dominated by planetesimal accretion from those where a significant fraction of the metallicity has been provided by the accretion of enriched nebular gas would allow us to constrain the relative importance and frequency of the two processes.

The inclusion of chemical reactions induced by the ionization environment to which the protoplanetary disk is exposed (Eistrup et al. 2016; Booth & Ilee 2019), particularly in compositional "reset" scenarios (Eistrup et al. 2016), will have more marked effects on our results, due to the more complex distribution of the different molecular species and their snowlines. Additional differences could also arise from the roles played by molecular species not included in our model, such as O_2 as the main carrier of O in the inner and intermediate disk and by HCN as the main solid-phase carrier of N in the outer disk (Eistrup et al. 2016). Also in this case, however, we would expect the large roles to be played by refractory and organic carriers of C, O, and S, and by gas as a carrier of N, to preserve the qualitative picture derived from our analysis.

4.4.2. Characterization of Planetary Growth, Migration, and Planetesimal Capture

The numerical approaches adopted for modeling the growth and migration of the giant planet we described in Section 2.2 provide an efficient way to explore the effects of different formation scenarios on the final planetary composition, as the change over time of the key quantities (mass and semimajor axis) depends only on their final values and the characteristic timescale of the involved process. This approach allows for capturing the fundamental aspects of the processes relevant to modeling the dynamical behavior of the protoplanetary disk and the planetesimal accretion by the giant planet, but it is not physically self-consistent.

The timescales of growth of the core and of the gaseous envelope and the migration rates during Type-I and Type-II migration are, in fact, dependent on each other and on the surrounding disk environment. Both the growth and the migration of the giant planet are linked to the characteristics of the disk environment and depend on parameters such as the disk viscosity, the gas accretion rate, the gas density profile, the pebble accretion rate, and the disk scale height; for recent discussions, see, e.g., Bitsch et al. (2015, 2019), Ida et al. (2018, 2020), and Tanaka et al. (2020).

Furthermore, the formation scenarios we have explored represent only a subset of the possible formation histories of giant planets, and they are focused specifically on the warm and hot giant planet populations that represent the ideal targets for spectroscopic investigations by future facilities like JWST and Ariel. Giant planets whose migration tracks end at larger distances from the host star, such as in the cases of the giant planets in our Solar System (e.g., Bitsch et al. 2015; Bosman et al. 2019; Öberg & Wordsworth 2019) and of directly imaged giant planets (Bowler et al. 2020), will be characterized by different elemental ratios than their hot and warm counterparts, even in cases of similar bulk metallicities.

Analogously, evolution tracks characterized by different values for the characteristic timescales τ_g in Equations (4) and (6), where we instead adopted a common τ_g value, would imply a different evolution over time of the collisional cross section of the migrating planet—and consequently, a different planetesimal accretion efficiency (see the results of the parametric study by Shibata et al. (2020), for different migration rates and planetary masses/radii). Moreover, different migration timescales are expected to affect the orbital region where the giant planet accretes planetesimals most efficiently due to the balance between the effects of aerodynamic drag and resonant capture (Shibata et al. 2020).

Specifically, slower migration rates are expected to decrease the accretion efficiency in the inner regions of the disk crossed by the giant planets with respect to faster migration rates (Shibata et al. 2020), as they provide more time for gas drag to act in regions where gas density is higher, with implications for the elemental ratios of the accreted material. Future investigations with more physically self-consistent treatments and larger sets of evolutionary tracks are therefore required in order to gain further insight regarding the compositional signatures of the formation process of giant planets.

However, we can already glean some insights about the general validity of the results we described by inspecting the radial behavior of the normalized elemental ratios of gas and solids in the protoplanetary disk as shown in Figure 9. As first evidenced by the early work of Öberg et al. (2011) in the case of the C/O ratio, the elemental ratios of gas and solids are characterized by opposite trends, with one possessing super-stellar values and the other sub-stellar values. While these trends are not strictly monotonic, the curves shown in Figure 9 never cross the value that represents the stellar elemental ratio.

Consequently, while evolutionary tracks different from those we considered will be characterized by different absolute values of the planetary metallicity (see also Shibata et al. 2020)

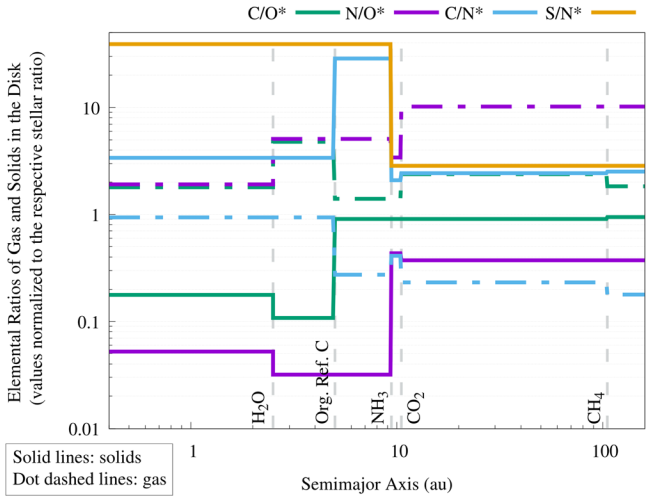

Figure 9. Elemental ratios of the gas (dotted–dashed lines) and the solids (solid lines) in the protoplanetary disk as a function of the radial distance from the star. Each elemental ratio is normalized to the relevant stellar elemental ratio.

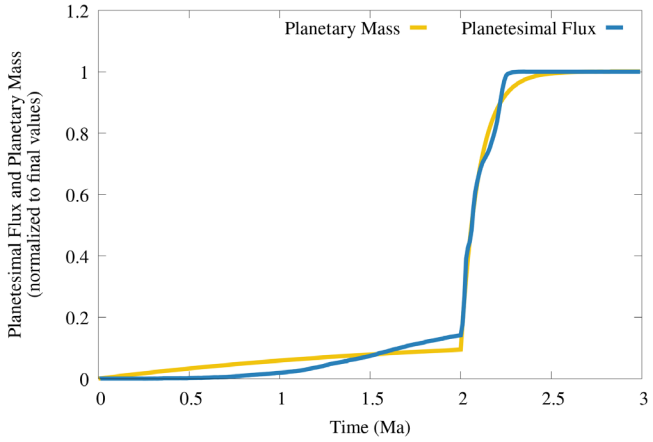

Figure 10. Mass growth and planetesimal accretion tracks, normalized to their final values, from the scenario where the giant planet starts forming at 19 au.

and elemental ratios with respect to the ones discussed in this work, the global picture depicted by Figures 4–9 should be qualitatively preserved.

Specifically, while the slopes of the curves in Figures 4–9 may change, giant planets whose metallicity is dominated by planetesimal accretion will still possess normalized ratios $C/N^* > C/O^* > N/O^*$, while giant planets whose metallicity is mainly contributed by the gas will possess $N/O^* > C/O^* > C/N^*$ (see Figure 9). Furthermore, due to the link between metallicity and migration highlighted by the results of Shibata et al. (2020) and this work, the differences between the values of these elemental ratios should still be proportional to the metallicity of the giant planet—and consequently, to the distance of its formation region from the host star.

4.4.3. Distribution of the Heavy Elements inside the Giant Planet

The elemental ratios we discussed have been computed under the assumption that all accreted heavy elements remain mixed within the gaseous envelope of the giant planet (see Section 2.4 and D'Angelo et al. 2014; Mordasini et al. 2015; Vazan et al. 2015; Podolak et al. 2020) and that the envelope and the atmosphere are compositionally homogeneous, either at the end of the formation process or after a few Gyr of interior evolution (see Section 2.4 and Vazan et al. 2015). Furthermore, the core of the giant planet is implicitly assumed to remain compositionally distinct from the envelope and not to contribute to the envelope metallicity, due to its erosion and dilution. Such a scenario, however, is only one of the possible end states of the giant planet.

It is possible that the interior of the giant planet is characterized instead by a layered structure, as recently suggested also for the case of Jupiter; for further discussion, see Debras & Chabrier (2019), Stevenson (2020), and references therein. If such a layered structure is established early in the life of the giant planet, it may prevent the envelope and the atmosphere from becoming compositionally homogeneous, and as a result, would cause them to be characterized by different elemental ratios. In other words, the atmosphere of the giant planet might reflect only the composition of the envelope outer layer, not of the giant planet as a whole. In this scenario, the atmospheric composition would constrain the gas and planetesimal accretion history of the giant planet during the tail of its formation process (see also Turrini et al. 2015) and provide a lower limit to the formation distance from the host star of the giant planet.

Another possibility is that material from the core significantly contributes to the envelope metallicity of giant planets by erosion and dilution; see Coradini et al. (2010), Helled (2018), Stevenson (2020), and references therein, as well as Öberg & Wordsworth (2019) for an in-depth discussion of the compositional implications. In such a scenario and without significant planetesimal accretion occurring during migration, the atmospheric elemental ratios of the giant planet could trace the original formation region of the planetary core (Öberg & Wordsworth 2019).

However, the results of Shibata et al. (2020) and this work indicate that a significant fraction of the envelope metallicity, if not the dominant one, arises from planetesimal accretion for giant planets experiencing large-scale migration while forming. As shown in Figure 10 and discussed by Podolak et al. (2020) for the case of nonmigrating giant planets, the bulk of the planetesimal accretion occurs during the runaway gas accretion phase. As a result, the atmospheric elemental ratio would reflect the composition of the region where the giant planet accreted the bulk of its envelope—and not that of the region, farther away from the host star, where the planetary core assembled (see also Figure 1 for a comparison between the mass growth and migration tracks).

5. Conclusions

In this work, we set out to investigate two main aspects of the link between the formation process and the composition and elemental ratios of giant planets. The first aspect was the impact of formation regions extending far from the host star and migration tracks crossing multiple compositional regions of the protoplanetary disk. The second one was the new information provided by elemental ratios involving N and S, in addition to C and O.

For a variety of initial orbital distances and migration tracks, we produced detailed *n*-body simulations of the interactions between growing and migrating giant planets and the surrounding planetesimal population. These simulations were coupled with a compositional model of the protoplanetary disk. The molecular abundances of the disk gas were inherited from the stellar core formation stage, while the elemental

abundances in the planetary solids were calibrated on all available observational data (from meteorites, comets, and the Sun, to the interstellar medium, circumstellar disks, and polluted white dwarfs).

Our results can be summarized as follows:

1. We confirm the proportionality between planetary migration and metallicity discussed by Shibata et al. (2020) in their study of the link between planetesimal accretion and migration. We show that the metallicity–migration correlation holds true also when the metallicity contribution of the accreted gas is accounted for, and that it shapes the abundance ratios of the high-Z elements of giant planets. This proportionality suggest that, the higher the migration, the higher the planetesimal accretion efficiency of giant planets—and the more markedly super-stellar their metallicities. This, in turn, suggests that the spread in the metallicity data of Jovian planets discussed by Thorngren et al. (2016), Wakeford et al. (2017), and Sing (2018) could be the reflection of different migration/planetesimal accretion histories.
2. The information provided by the C/O ratio is quite limited in cases of giant planets that acquire the bulk of their C and O beyond the CO_2 snowline, where the main gaseous carriers of these elements are CH_4 and CO.

   In the case of gas-dominated giant planets, the C/O ratio show values greater than one, due to CH_4 increasing the C/O ratio of the gas with respect to the value of one otherwise set by CO. On the other hand, for solid-enriched giant planets, the C/O ratio shows slightly sub-stellar values.

   In both cases, however, the C/O ratio is essentially constant with the initial distance of the planetary seed, therefore providing little or no clue with regard to the formation region. More marked changes in the C/O values are seen, in both cases, for giant planets growing within the CO_2 snowline, but even in these cases, the C/O values do not vary by more than 10%–20%.

   Such limited changes in the C/O values are smaller than the accuracy of current retrieval tools (e.g., Barstow et al. 2020); as a result, the C/O ratios of the different migration scenarios we considered in this work would be observationally indistinguishable from each other. Consequently, the C/O ratio would not yield any insight regarding the formation region and migration track of the giant planet.
3. The degeneracy in the information provided by C/O can be broken through the use of the C/N and N/O ratios, which provide stronger constraints on the formation region and extent of migration of giant planets (see Figure 5).

   We find that the N/O ratio significantly grows with migration for gas-dominated/low-metallicity giant planets and decreases for solid-enriched/high-metallicity ones.

   This is because the bulk of O is trapped into solids already in the inner regions of the protoplanetary disk, while the bulk of N remains in gaseous form until the outermost regions. The C/N ratio shows the opposite behavior for similar reasons, i.e., due to the earlier incorporation of the bulk of C into solids with respect to N.
4. The behavior of the C/N and N/O elemental ratios is fundamentally determined by the solidly established volatility of N, which causes the N content of giant planets to grow slower with planetesimal accretion than that of the other elements. The farther the giant planets start their migration from the host star, the more their C/N and N/O ratios diverge from the stellar values.

   For giant planets starting their formation increasingly close to the host star, the C/N ratio of giant planets will converge to the stellar value, as both C and N will be in gas form in the inner few au of protoplanetary disks (see Figure 5).
5. The N/O ratios of gas-dominated and solid-enriched giant planets, however, will be significantly different even for very small migration distances, as a fraction of O is always trapped into rocks (see Figure 5).

   Hence, if gas is the main source of high-Z elements for a giant planet, its N/O value will remain super-stellar. If the envelope of the giant planet is instead significantly enriched by solids, its N/O value will reach the stellar value at most.

   Due to the monotonic trends of the planetary C/N and N/O ratios, giant planets accreting gas and solids in different regions of the disk will not share the same values of these elemental ratios even if they share the same overall metallicity.
6. The S/N ratio provides a direct window into the metallicity of giant planets. Specifically, given that the bulk of S is sequestered early into solids while the bulk of N remains in gas phase, the S/N ratio can be used as a proxy into the amount of solid material giant planets accrete as planetesimals during their formation history. This allows us to validate the indirect estimates of the metallicity based on the mass–radius relationship of giant planets, but can in principle also allow for the metallicity contributions of gas and solids to be separated in order to obtain a more complete picture of the formation history of giant planets.
7. The C/O, C/N, N/O, and S/N ratios normalized to their stellar values (indicated with the superscript *) reveal that solid-enriched giant planets will be characterized by $C/N^* > C/O^* > N/O^*$. Gas-dominated giant planets will instead be characterized by $N/O^* > C/O^* > C/N^*$. The farther away from the star the giant planet started its formation path, the greater the difference between the three normalized ratios.

   Moreover, giant planets for which planetesimal accretion is the main source of metallicity (as in the case of large-scale migration) will have $S/N^* > C/N^*$. Giant planets for which both gas and solids contribute to the metallicity will instead have $C/N^* > S/N^*$, with the contrast between the two values being higher the less the solids contribute to metallicity.

   These trends depend on the fact that the bulk of S is incorporated into solids in protoplanetary disks before the bulk of O and C, which in turn are incorporated into solids before the bulk of N. As such, the comparison between S/N^* and C/N^* can be used to discriminate between high-metallicity giant planets that accreted nebular gas enriched in heavy elements (Booth & Ilee 2019) versus those for which planetesimal accretion was the dominant source of heavy elements.

8. Finally, similarly to the case of the normalized metallicities values adopted by Thorngren et al. (2016), the use of normalized elemental ratios (not necessarily limited to C/N, N/O, C/O, and S/N) removes the intrinsic compositional variability between different planetary systems, due to the specific elemental budgets of their protoplanetary disks. This, in turn, opens up the possibility of more reliable comparisons between the respective formation and migration histories of giant planets orbiting different stars.

   Furthermore, any element whose main carrier is characterized by a volatility lower than or similar to that of S can be used to compute normalized elemental ratios with respect to N and gain insight regarding the source of the planetary metallicity (Turrini et al. 2018). The use of normalized elemental ratios therefore allows us to compare the constraint on the metallicity derived for different giant planets using different low-volatility elements (e.g., S/N^*, Al/N^*, Na/N^*, Cr/N^*).

This first work illustrates the potential of elemental ratios involving sulfur and nitrogen in considerably expanding the toolkit available to probe the formation history of giant exoplanets. In subsequent works, we will test the predictive power of our tracers against different protoplanetary disk chemical histories, and explore their application to exoplanetary atmospheres as probes into the formation history of exoplanets.

The authors wish to thank the two anonymous referees for their comments and suggestions, which improved the presentation of the work and the discussion of its results and implications. The authors also wish to thank Nadia Balucani, Maria Teresa Capria, Cecilia Ceccarelli, Marco Fulle, Francesco Marzari, Elenia Pacetti, Yamila Miguel, and Michiel Min, as well as the Planetary Formation Working Group of the Ariel Consortium, for useful discussions and comments during the development of this work. D. T., E. S., S. F., S. M., R. P., and D. F. gratefully acknowledge the support of the Italian Space Agency (ASI) through the ASI-INAF contract 2018-22-HH.0, and the Italian National Institute of Astrophysics (INAF) through the INAF Main Stream project "ARIEL and the astrochemical link between circumstellar disks and planets" (CUP C54I19000700005). D. F. acknowledges support from the INAF Main Stream project "Protoplanetary disks seen through the eyes of new-generation instruments" (CUP: C54I19000600005). O.P. is funded through the Royal Society Dorothy Hodgkin Fellowship DH140243. M. K. was supported by the University of Tartu ASTRA project 2014-2020.4.01.16-0029 KOMEET, financed by the EU European Regional Development Fund. The computation resources for this work were supplied by the Genesis cluster at INAF-IAPS. This research has made use of the Wolfram Alpha "Computational Intelligence" service and of the NASA Astrophysics Data System Bibliographic Services. This project has received funding from the European Research Council under the European Union's Horizon 2020 research and innovation program (ERC grant agreement No. 758892, ExoAI), the European Union's Seventh Framework Programme (FP7/2007-2013), and the ExoLight project (ERC grant agreement No. 617119). Furthermore, the authors acknowledge funding by the Science and Technology Funding Council (STFC) grants: ST/K502406/1, ST/P000282/1, ST/P002153/1, ST/S002634/1, and ST/T001836/1. This project received support from the UCL London–Rome Cities Partnerships Program: ASI grant No. 2018.22.HH.O.

ORCID iDs

D. Turrini https://orcid.org/0000-0002-1923-7740
E. Schisano https://orcid.org/0000-0003-1560-3958
S. Fonte https://orcid.org/0000-0002-3911-7340
S. Molinari https://orcid.org/0000-0002-9826-7525
R. Politi https://orcid.org/0000-0002-9793-9780
D. Fedele https://orcid.org/0000-0001-6156-0034
O. Panić https://orcid.org/0000-0002-6648-2968
M. Kama https://orcid.org/0000-0003-0065-7267
Q. Changeat https://orcid.org/0000-0001-6516-4493
G. Tinetti https://orcid.org/0000-0001-6058-6654

References

ALMA Partnership, Brogan, C. L., Pérez, L. M., et al. 2015, ApJL, 808, L3
Altwegg, K., Balsiger, H., & Fuselier, S. A. 2019, ARA&A, 57, 113
Andrews, S. M., Huang, J., Pérez, L. M., et al. 2018, ApJL, 869, L41
Ansdell, M., Williams, J. P., Trapman, L., et al. 2018, ApJ, 859, 21
Armitage, P. J. 2009, Astrophysics of Planet Formation (Cambridge: Cambridge Univ. Press)
Asplund, M., Grevesse, N., Sauval, A. J., & Scott, P. 2009, ARA&A, 47, 481
Atreya, S. K., Crida, A., Guillot, T., et al. 2018, in Saturn in the 21st Century, ed. K. H. Baines et al. (Cambridge: Cambridge Univ. Press), 5
Bardyn, A., Baklouti, D., Cottin, H., et al. 2017, MNRAS, 469, S712
Barstow, J. K., Changeat, Q., Garland, R., et al. 2020, MNRAS, 493, 4884
Bergin, E. A., Blake, G. A., Ciesla, F., Hirschmann, M. M., & Li, J. 2015, PNAS, 112, 8965
Bianchi, E., Codella, C., Ceccarelli, C., et al. 2019, MNRAS, 483, 1850
Bitsch, B., Izidoro, A., Johansen, A., et al. 2019, A&A, 623, A88
Bitsch, B., Lambrechts, M., & Johansen, A. 2015, A&A, 582, A112
Booth, R. A., & Ilee, J. D. 2019, MNRAS, 487, 3998
Bosman, A. D., Cridland, A. J., & Miguel, Y. 2019, A&A, 632, L11
Bowler, B. P., Blunt, S. C., & Nielsen, E. L. 2020, AJ, 159, 63
Brasser, R., Duncan, M. J., & Levison, H. F. 2007, Icar, 191, 413
Britt, D. T., Yeomans, D., Housen, K., & Consolmagno, G. 2002, in Asteroids III, ed. W. F. Bottke, Jr. et al. (Tucson, AZ: Univ. Arizona Press), 485
Carry, B. 2012, P&SS, 73, 98
Chambers, J. E. 1999, MNRAS, 304, 793
Changeat, Q., Al-Refaie, A., Mugnai, L. V., et al. 2020, AJ, 160, 80
Changeat, Q., Edwards, B., Al-Refaie, A. F., et al. 2020, AJ, 160, 260
Coradini, A., Magni, G., & Turrini, D. 2010, SSRv, 153, 411
Cowan, N. B., Greene, T., Angerhausen, D., et al. 2015, PASP, 127, 311
Cresswell, P., & Nelson, R. P. 2008, A&A, 482, 677
Cridland, A. J., van Dishoeck, E. F., Alessi, M., & Pudritz, R. E. 2019, A&A, 632, A63
D'Angelo, G., Durisen, R. H., & Lissauer, J. J. 2010, in Exoplanets, ed. S. Seager (Tucson, AZ: Univ. Arizona Press), 319
D'Angelo, G., Weidenschilling, S. J., Lissauer, J. J., & Bodenheimer, P. 2014, Icar, 241, 298
D'Angelo, G., Weidenschilling, S. J., Lissauer, J. J., & Bodenheimer, P. 2021, Icar, 355, 114087
Debras, F., & Chabrier, G. 2019, ApJ, 872, 100
Doyle, A. E., Young, E. D., Klein, B., Zuckerman, B., & Schlichting, H. E. 2019, Sci, 366, 356
Drozdovskaya, M. N., van Dishoeck, E. F., Rubin, M., Jørgensen, J. K., & Altwegg, K. 2019, MNRAS, 490, 50
Drummond, B., Hébrard, E., Mayne, N. J., et al. 2020, A&A, 636, A68
Edwards, B., Rice, M., Zingales, T., et al. 2018, ExA, 47, 29
Eistrup, C., Walsh, C., & van Dishoeck, E. F. 2016, A&A, 595, A83
Eistrup, C., Walsh, C., & van Dishoeck, E. F. 2018, A&A, 613, A14
Facchini, S., van Dishoeck, E. F., Manara, C. F., et al. 2019, A&A, 626, L2
Fedele, D., Carney, M., Hogerheijde, M. R., et al. 2017, A&A, 600, A72
Fedele, D., Tazzari, M., Booth, R., et al. 2018, A&A, 610, A24
Fegley, B., & Schaefer, L. 2010, ASSP, 16, 347
Fisher, C., & Heng, K. 2018, MNRAS, 481, 4698
Fontana, A., & Marzari, F. 2016, A&A, 589, A133
Fortier, A., Alibert, Y., Carron, F., Benz, W., & Dittkrist, K. M. 2013, A&A, 549, A44

Gratton, R., Ligi, R., Sissa, E., et al. 2019, A&A, 623, A140
Greene, T. P., Line, M. R., Montero, C., et al. 2016, ApJ, 817, 17
Guilluy, G., Gressier, A., Wright, S., et al. 2021, AJ, 161, 19
Hahn, J. M., & Malhotra, R. 2005, AJ, 130, 2392
Hayashi, C. 1981, PThPS, 70, 35
Helled, R. 2018, The Interiors of Jupiter and Saturn (Oxford, UK: Oxford Univ. Press), 175
Ida, S., Muto, T., Matsumura, S., & Brasser, R. 2020, MNRAS, 494, 5666
Ida, S., Tanaka, H., Johansen, A., Kanagawa, K. D., & Tanigawa, T. 2018, ApJ, 864, 77
Isella, A., Guidi, G., Testi, L., et al. 2016, PhRvL, 117, 251101
Isnard, R., Bardyn, A., Fray, N., et al. 2019, A&A, 630, A27
Johnson, T. V., Mousis, O., Lunine, J. I., & Madhusudhan, N. 2012, ApJ, 757, 192
Jorda, L., Gaskell, R., Capanna, C., et al. 2016, Icar, 277, 257
Jurić, M., & Tremaine, S. 2008, ApJ, 686, 603
Kama, M., Shorttle, O., Jermyn, A. S., et al. 2019, ApJ, 885, 114
Kinoshita, H., Yoshida, H., & Nakai, H. 1991, CeMDA, 50, 59
Klahr, H., & Schreiber, A. 2016, in IAU Symp. 318, Asteroids: New Observations, New Models, ed. S. R. Chesley et al. (Cambridge: Cambridge Univ. Press), 1
Kokubo, E., & Ida, S. 2000, Icar, 143, 15
Laskar, J., & Petit, A. C. 2017, A&A, 605, A72
Le Roy, L., Altwegg, K., Balsiger, H., et al. 2015, A&A, 583, A1
Limbach, M. A., & Turner, E. L. 2015, PNAS, 112, 20
Lissauer, J. J., Hubickyj, O., D'Angelo, G., & Bodenheimer, P. 2009, Icar, 199, 338
Lodders, K. 2010, ASSP, 16, 379
Long, F., Pinilla, P., Herczeg, G. J., et al. 2018, ApJ, 869, 17
MacDonald, R. J., & Madhusudhan, N. 2017a, MNRAS, 469, 1979
MacDonald, R. J., & Madhusudhan, N. 2017b, ApJL, 850, L15
Madhusudhan, N. 2019, ARA&A, 57, 617
Madhusudhan, N., Agúndez, M., Moses, J. I., & Hu, Y. 2016, SSRv, 205, 285
Manara, C. F., Morbidelli, A., & Guillot, T. 2018, A&A, 618, L3
Marboeuf, U., Thiabaud, A., Alibert, Y., Cabral, N., & Benz, W. 2014a, A&A, 570, A35
Marboeuf, U., Thiabaud, A., Alibert, Y., Cabral, N., & Benz, W. 2014b, A&A, 570, A36
Marzari, F. 2018, A&A, 611, A37
Min, M., Ormel, C. W., Chubb, K., Helling, C., & Kawashima, Y. 2020, A&A, 642, A28
Morbidelli, A., & Raymond, S. N. 2016, JGRE, 121, 1962
Mordasini, C., Alibert, Y., & Benz, W. 2009, A&A, 501, 1139
Mordasini, C., Mollière, P., Dittkrist, K. M., Jin, S., & Alibert, Y. 2015, IJAsB, 14, 201
Mordasini, C., van Boekel, R., Mollière, P., Henning, T., & Benneke, B. 2016, ApJ, 832, 41
Nagasawa, M., Tanaka, K. K., Tanaka, H., et al. 2019, ApJ, 871, 110
Nelson, R. P. 2018, in International Publishing, ed. H. J. Deeg & J. A. Belmonte (Cham: Springer International Publishing), 2287
Öberg, K. I., Qi, C., Fogel, J. K. J., et al. 2011, ApJ, 734, 98
Öberg, K. I., & Wordsworth, R. 2019, AJ, 158, 194
Palme, H., Lodders, K., & Jones, A. 2014, in Planets, Asteriods, Comets and The Solar System, Vol. 2 ed. A. M. Davis (Amsterdam: Elsevier), 15
Palme, H., & Zipfel, J. 2017, in Assessment and Mitigation of Asteroid Impact Hazards, ed. J. M. Trigo-Rodríguez, M. Gritsevich, & H. Palme (Cham: Springer)
Panić, O., & Min, M. 2017, MNRAS, 467, 1175
Pinhas, A., Madhusudhan, N., Gandhi, S., & MacDonald, R. 2018, MNRAS, 482, 1485
Pirani, S., Johansen, A., Bitsch, B., Mustill, A. J., & Turrini, D. 2019, A&A, 623, A169
Piso, A.-M. A., Pegues, J., & Öberg, K. I. 2016, ApJ, 833, 203
Podolak, M., Haghighipour, N., Bodenheimer, P., Helled, R., & Podolak, E. 2020, ApJ, 899, 45
Pollack, J. B., Hollenbach, D., Beckwith, S., et al. 1994, ApJ, 421, 615
Porco, C. C., Baker, E., Barbara, J., et al. 2005, Sci, 307, 1237
Rein, H., & Tamayo, D. 2015, MNRAS, 452, 376
Rubin, M., Altwegg, K., Balsiger, H., et al. 2019, MNRAS, 489, 594
Rubin, M., Engrand, C., Snodgrass, C., et al. 2020, SSRv, 216, 102
Scott, E. R. D. 2007, AREPS, 35, 577
Scott, P., Asplund, M., Grevesse, N., Bergemann, M., & Sauval, A. J. 2015a, A&A, 573, A26
Scott, P., Grevesse, N., Asplund, M., et al. 2015b, A&A, 573, A25
Semenov, D., Henning, T., Helling, C., Ilgner, M., & Sedlmayr, E. 2003, A&A, 410, 611
Shibata, S., Helled, R., & Ikoma, M. 2020, A&A, 633, A33
Shibata, S., & Ikoma, M. 2019, MNRAS, 487, 4510
Sing, D. K. 2018, in Astrophysics of Exoplanetary Atmospheres: 2nd Advanced School on Exoplanetary Science, ed. V. Bozza, L. Mancini, & A. Sozzetti (Cham: Springer International Publishing), 3
Stevenson, D. J. 2020, AREPS, 48, 465
Szulágyi, J., Masset, F., Lega, E., et al. 2016, MNRAS, 460, 2853
Tanaka, H., Murase, K., & Tanigawa, T. 2020, ApJ, 891, 143
Thiabaud, A., Marboeuf, U., Alibert, Y., et al. 2014, A&A, 562, A27
Thorngren, D. P., Fortney, J. J., Murray-Clay, R. A., & Lopez, E. D. 2016, ApJ, 831, 64
Tinetti, G., Drossart, P., Eccleston, P., et al. 2018, ExA, 46, 135
Tsiaras, A., Waldmann, I. P., Zingales, T., et al. 2018, AJ, 155, 156
Turrini, D. 2014, P&SS, 103, 82
Turrini, D., Coradini, A., & Magni, G. 2012, ApJ, 750, 8
Turrini, D., Magni, G., & Coradini, A. 2011, MNRAS, 413, 2439
Turrini, D., Marzari, F., Polychroni, D., & Testi, L. 2019, ApJ, 877, 50
Turrini, D., Miguel, Y., Zingales, T., et al. 2018, ExA, 46, 45
Turrini, D., Nelson, R. P., & Barbieri, M. 2015, ExA, 40, 501
Turrini, D., & Svetsov, V. 2014, Life, 4, 4
Turrini, D., Zinzi, A., & Belinchon, J. A. 2020, A&A, 636, A53
Vazan, A., Helled, R., Kovetz, A., & Podolak, M. 2015, ApJ, 803, 32
Venot, O., Drummond, B., Miguel, Y., et al. 2018, ExA, 46, 101
Wakeford, H. R., Sing, D. K., Kataria, T., et al. 2017, Sci, 356, 628
Walsh, K. J., Morbidelli, A., Raymond, S. N., O'Brien, D. P., & Mandell, A. M. 2011, Natur, 475, 206
Ward, W. R. 1981, Icar, 47, 234
Weidenschilling, S. J. 2008, PhST, 130, 014021
Wisdom, J., & Holman, M. 1991, AJ, 102, 1528
Woitke, P., Helling, C., Hunter, G. H., et al. 2018, A&A, 614, A1
Zinzi, A., & Turrini, D. 2017, A&A, 605, L4